Neogene tectono-stratigraphic evolution of the intermontane Tarom Basin: insights into basin filling and plateau building processes along the northern margin of the Iranian Plateau...

Paolo Ballato
Università Degli Studi Roma Tre

Jamshid Hassanzadeh
California Institute of Technology

Giovanni Vezzoli
Università degli Studi di Milano-Bicocca

Majid mirzaie ataabadi
University of Zanjan

Tectonics

RESEARCH ARTICLE

10.1029/2020TC006254

Key Points:

- The red beds of the Tarom Basin are > ~16.2 to < ~7.6-My-old and are stratigraphically equivalent to the Upper Red Formation
- Over the last 38-36 Ma the basin experienced alternating stages of internal and external drainage without being integrated in the plateau
- Deep seated processes rather than shortening and thickening are responsible for the vertical growth of the Iranian Plateau margin

Correspondence to:

M. Paknia,
Mohammad.Paknia@uniroma3.it

Citation:

Paknia, M., Ballato, P., Heidarzadeh, G., Cifelli, F., Hassanzadeh, J., Vezzoli, G., et al. (2021). Neogene tectono-stratigraphic evolution of the intermontane Tarom Basin: Insights into basin filling and plateau building processes along the northern margin of the Iranian Plateau (Arabia-Eurasia collision zone). *Tectonics*, *40*, e2020TC006254. https://doi.org/10.1029/2020TC006254

Received 25 APR 2020
Accepted 19 JAN 2021

Neogene Tectono-Stratigraphic Evolution of the Intermontane Tarom Basin: Insights Into Basin Filling and Plateau Building Processes Along the Northern Margin of the Iranian Plateau (Arabia-Eurasia Collision Zone)

M. Paknia[1], P. Ballato[1], G. Heidarzadeh[2], F. Cifelli[1], J. Hassanzadeh[3], G. Vezzoli[4], M. Mirzaie Ataabadi[5], M. R. Ghassemi[6], and M. Mattei[1]

[1]Department of Science, University of Roma Tre, Rome, Italy, [2]Institute of Earth and Environmental Sciences, University of Potsdam, Potsdam, Germany, [3]Division of Geological & Planetary Sciences, California Institute of Technology Pasadena, Pasadena, CA, USA, [4]Department of Earth and Environmental Sciences, University of Milano-Bicocca, Milan, Italy, [5]Department of Geology, Faculty of Science, University of Zanjan, Zanjan, Iran, [6]Research Institute for Earth Sciences, Geological Survey of Iran, Tehran, Iran

Abstract The intermontane Tarom Basin of NW Iran (Arabia-Eurasia collision zone) is located at the transition between the Iranian Plateau (IP) to the SW and the Alborz Mountains to the NE. This basin was filled by upper Cenozoic synorogenic red beds that retain first-order information on the erosional history of adjacent topography, the vertical growth of the plateau margin and its orogen perpendicular expansion. Here, we perform a multidisciplinary study including magnetostratigraphy, sedimentology, geochronology and sandstone petrography on these red beds. Our data show that Eocene arc volcanism in the region terminated at 38-36 Ma, while intrabasinal synorogenic sedimentation (endorheic conditions) occurred from at least 16.2 to <7.6 Ma, implying that the red beds are stratigraphically equivalent to the Upper Red Formation. After 7.6 Ma, the basin experienced intrabasinal deformation, uplift and erosion with the establishment of external drainage. Fluvial connectivity with the Caspian Sea, however, was interrupted by at least four episodes of basin aggradation. During endorheic conditions, the basin fill did not reach the elevation of the plateau interior and hence the Tarom Basin was never integrated into the plateau. Furthermore, our provenance data indicate that the northern margin of the basin (Alborz Mountains) experienced a greater magnitude of Miocene deformation and erosional exhumation than the southern one (IP margin). This agrees with recent Moho depth estimates, suggesting that crustal shortening and thickening cannot be responsible for the vertical growth of the northern margin of the IP, and hence surface uplift must have been driven by deep-seated processes.

1. Introduction

Orogenic plateaus are vast and elevated morphotectonic features, which provide the unique opportunity to decipher the interplay between shallow, deep-seated and surface processes, and their influences on Earth's landscape at various timescales (e.g., Dewey et al., 1988; Isacks, 1988; Molnar et al., 1993). They often contain internally drained basins that have coalesced and have been filled with thick sedimentary deposits and hence retain insights into orogenic, erosional and geodynamic processes (e.g., Alonso et al., 1990; Carroll et al., 2010; Horton et al., 2012; Meyer et al., 1998; Pingel et al., 2019a; Sobel et al., 2003; Strecker et al., 2009). One of the most accepted plateau-building model predicts that reduced fluvial connectivity promotes basin filling with sediments, inhibits intrabasinal faulting, and triggers the outward propagation of the deformation fronts. Combined, these processes are thought to be responsible for the lateral (orogen perpendicular) plateau expansion through the integration of new sectors of the foreland into the plateau realm. (Garcia Castellanos et al., 2007; Sobel et al., 2003). The application of this model, however, is not straightforward mostly because the interplay between tectonic and surface processes may trigger a different scenario. This includes basin excavation and erosion with the destruction of the typical plateau morphology (e.g., Heidarzadeh et al., 2017; Strecker et al., 2009). Therefore, while the sedimentary basins in the plateau interior are tectonically stable up to time scales of few 10^7 years (e.g., Alonso et al., 1990; Bush et al., 2016), intermontane basins at the transition with the foreland may experience a more complex evolution including several episodes of basin filling and plateau integration, fluvial incision and tectonic deformation at shorter time scales (10^5 to few 10^6 years; e.g., Ballato et al., 2019; Pingel et al., 2019a; T. Schildgen et al., 2016; Streit et al., 2015; Tofelde et al., 2017). Thus, these transitional basins hold precious information on the growth of the plateau margin, the evolution of adjacent mountain ranges, the sediment routing systems and the connectivity history among different sedimentary basins.

The NW-SE-oriented Iranian Plateau (IP) is located in the Arabia-Eurasia collision zone and represents the second largest collisional plateau in elevation and size after Tibet (Figure 1; see Hatzfeld and Molnar [2010] for a comparison). Like Tibet, the IP formed over the upper plate (Eurasia) of a northward, MesoCenozoic subduction system that led to the closure of the Neo-Tethys ocean (Agard et al., 2011) and the collision of Eurasia with continents of Gondwanaland (India and Arabia, for Tibet and Iran, respectively; Hatzfeld & Molnar, 2010). The IP is parallel to the Zagros orogenic belt and is characterized by high elevation (average elevation is ~1,800 m), relatively low internal topographic relief (few hundred of meters), dry climatic conditions, endorheic sedimentary basins in its interior (three out of six major basins are currently internally drained), and steep and dissected flanks bounded by major reverse faults (Figure 1; Ballato et al., 2013, 2017; Heidarzadeh et al., 2017). The timing of the vertical growth of the plateau is unknown, however, the occurrence of lower Miocene shallow-water marine limestone of the Qom Formation within the plateau interior indicates that surface uplift must be younger than ~17 Ma (e.g., Ballato et al., 2017; Morley et al., 2009). In Central Iran, the northern margin of the IP is marked by a sharp boundary with the adjacent foreland, which comprises the Central Iranian Block (Figure 1). Conversely, in NW Iran, the IP approaches the Caspian Sea and it is separated from the intracontinental Alborz and Talesh mountains by an elongated, NW-SE oriented intermontane basin called Tarom Basin. Currently, this basin is drained by the Qezel-Owzan River (QOR), the second largest river in Iran that flows from the interior of the IP to the Caspian Sea. The basin is composed of post Eocene, synorogenic red beds that offer the opportunity to investigate puzzling aspects of this collision zone, such as: the timing and mechanisms of plateau margin uplift, its lateral expansion (i.e., the possible incorporation of the intermontane Tarom Basin in the plateau realm) and the link with the adjacent growing Alborz Mountains. For this purpose, we have performed a multidisciplinary study including the characterization of the depositional environments, the sediment provenance areas and the depositional age of the post Eocene synorogenic red beds. Our magnetostratigraphic analysis and new zircon U-Pb ages document that the widespread Eocene arc volcanism in NW Iran terminated at ~38-36 Ma, while the deposition of the red beds started not later than ~16.2 Ma and lasted at least until ~7.6 Ma during the growth of the adjacent basin margins. Further, we document the occurrence of alternating periods of efficient and limited fluvial connectivity and we discuss the mechanisms that may have led to the growth of the IP margin in this sector of the Arabia-Eurasia collision zone.

1.1. Geological Setting

The Tarom Basin is an intermontane basin located along the northern margin of the IP between the western Alborz Mountains to the NE and the Tarom range to the SW (Arabia-Eurasia collision zone; Figure 1). The western Alborz Mountains consist of Precambrian crystalline basement rocks, Paleozoic and Mesozoic marine deposits, Eocene volcanics, volcaniclastics, and intrusives of variable age (Figure 1). This assemblage indicates a complex history of deformation, exhumation, metamorphism, magmatism, subsidence and sedimentation (Figure 1e) that includes: (1) development of a metamorphic basement during the Neoproterozoic Pan-African Orogeny (e.g., Hassanzadeh et al., 2008); (2) deposition of unconformable carbonate and clastic marine deposits of Precambrian and Paleozoic age associated with the opening the Paleo-Tethys Ocean (e.g., B. K. Horton et al., 2008); (3) occurrence of the Triassic Cimmerian Orogeny (e.g., Omrani et al., 2013; Zanchi et al., 2009); (4) renewed Mesozoic subsidence with the sedimentation of postorogenic clastic sediments of the Shemshak Formation (e.g., Wilmesen et al., 2009; Zanchi et al., 2009); (5) deposition of shallow-to deep-marine middle to Upper Jurassic sediments during the opening of the South Caspian Basin (e.g., Brunet et al., 2003); (6) Cretaceous thermal subsidence and marine sedimentation (Brunet et al., 2003); (7) late Cretaceous to Paleocene deformation and exhumation during a regional compressional event (e.g., Guest, Axen et al., 2006; Madanipour et al., 2017; Yassaghi & Madanipour, 2008); (8) deposition of Eocene volcaniclastics in a backarc system associated with the rollback of the Neo-Tethyan oceanic slab (Ballato et al., 2011, 2013; Guest, Axen et al., 2006; Rezaeian et al., 2012; Verdel et al., 2011) and finally, (9) contractional deformation and exhumation during the final closure of the Neo-Tethys ocean and the collision between Eurasia and Arabia starting from the latest Eocene-earliest Oligocene (e.g., Ballato et al., 2011, 2013, Guest, Axen et al., 2006; Guest, Stockli et al., 2006; Koshnaw et al., 2018; Madanipour et al., 2017, 2018; Mouthereau et al., 2012; Pirouz et al., 2017; Rezaeian et al., 2012). This final collisional led to development of a narrow, double-verging mountain belt with up to 4 km of topographic relief that represents an effective orographic barrier to moist air masses sourced from the Caspian Sea (Figure 1; Ballato et al., 2015 and references therein). Available low-temperature thermochronology data for the western Alborz Mountains document slow exhumation from the early Oligocene followed by a middle Miocene acceleration (Madanipour et al., 2017). Currently, the range accommodates left-lateral shearing between the Caspian Sea and Central Iran (Djamour et al., 2010) and is characterized by the occurrence of few seismogenic faults including the strike-slip Rudbar Fault, which ruptured in 1990 leading to the catastrophic Mw 7.3 earthquake (Berberian & Walker, 2010).

The Tarom range consists of an at least 4-km-thick pile of Eocene volcanic and volcanoclastic rocks of the Karaj Formation (Figures 1 and 2; Stocklin & Eftekharnezhad, 1969) that were deposited in the backarc of the Neo-Tethys subduction zone between ∼55 and 38-36 Ma (Ballato et al., 2011, 2013; Guest, Axen et al., 2006; Rezaeian et al., 2012; Verdel et al., 2011). This was associated with the emplacement of Upper Eocene (∼41-37 Ma) shallow intrusive rocks (Castro et al., 2013; Nabatian et al., 2014). In the Tarom range these deposits form a broad, south-verging anticline (Heidarzadeh et al., 2017) with smaller scale anticline-syncline pairs (Figure 1), cut by minor high angle (both south and north dipping) reverse faults, locally with a lateral component. Available low-temperature thermochronology data indicate that uplift and exhumation of the Tarom range could have started around the latest Eocene-earliest Oligocene and resumed most likely during the last ∼5 Ma (Rezaeian et al., 2012).

1.2. Regional Stratigraphy

The Tarom Basin was filled by post Eocene red beds that rest with an angular unconformity onto Eocene volcanic rocks and volcanoclastic units of the Karaj Formation (Figure 2). The stratigraphic position of the red beds is unknown, mostly because the late Oligocene-early Miocene marine transgression that led to the widespread deposition of the shallow-water marine limestones of the Qom Formation (Reuter et al., 2009) did not reach the Tarom Basin. These marine deposits are sandwiched between the clastic deposits of the Lower Red (LRF; supposed Oligocene age) and Upper Red (URF, Miocene) formations and represent a regional marker that can be followed along the southern margin of the Eurasian plate (Figure 1e; see Gansser [1958] for a first exhaustive description of these units). Therefore, their absence in Tarom Basin does not allow differentiating the stratigraphic position of the red beds, which have been considered either Oligo-Miocene (R. G. Davies, 1977; Stocklin & Eftekharnezhad, 1969) or Miocene in age (Figures 1 and 2; Amini, 1969).

The LRF and the URF are exposed virtually everywhere along the southern margin of the Eurasian plate, where they have a thickness varying from a few hundreds to a few thousands of meters (Figure 1e). These red beds are characterized by a variable amount of sandstones, conglomerates, mudstones, evaporites and locally volcanics, and are mostly considered synorogenic sediments associated with collisional deformation (e.g., Ballato et al., 2008, 2011, 2017; Madanipour et al., 2017; Morley et al., 2009; Rezaeian, et al., 2012). Lithologically, the LRF is rather heterogeneous, while the URF seems to have more uniform characteristics, and hence has been differentiated into three units (M1, M2, and M3; e.g., Davoudzadeh et al., 1997). Units M1 and M3 are generally dominated by mudstones and evaporites with a variable amount of sandstones and conglomerates while Unit M2 is characterized by abundant sandstones. The URF is superseded by supposedly Pliocene conglomerates (Hezadarreh Formation; Rieben et al., 1955) that are generally thought to mark an intensification of collisional deformation (e.g., Rezaeian, et al., 2012; Madanipour et al., 2017). These conglomerates, however, are diachronous and their age depends on their position with respect to the coeval active mountain fronts. For example, in the southern Alborz Mountains (Ballato et al., 2008) and in the interior of the IP (Tavaq Conglomerates, Great Pari Sedimentary Basin; Ballato et al., 2017) conglomeratic deposition started at ∼7.5 and ∼10.7 Ma, respectively. Locally, they can be unconformable onto the URF or older strata (Figure 1e).

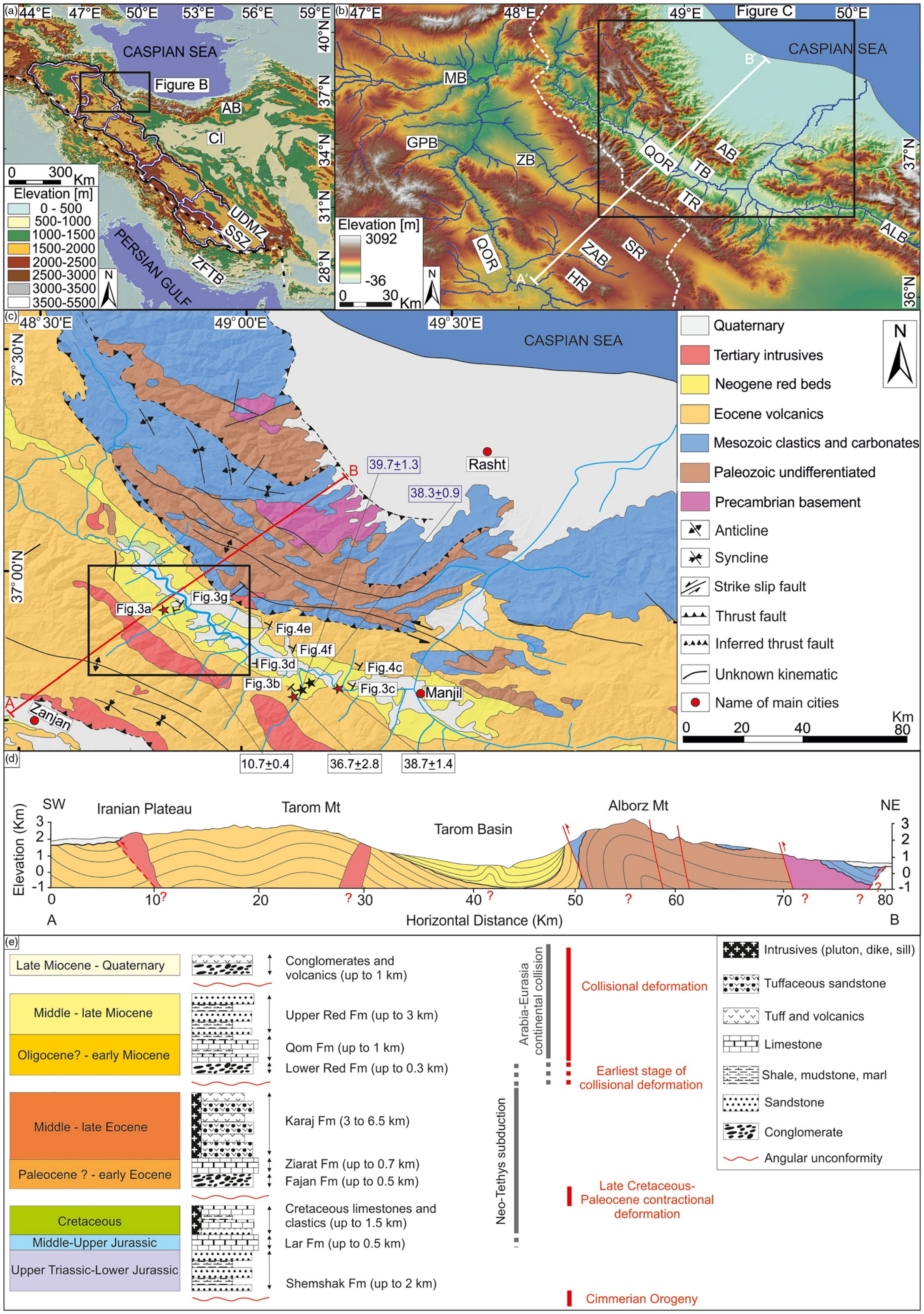
(a)
44°E
47°E
50°E
53°E
56°E
59°E
40°N
37°N
34°N
31°N
28°N
CASPIAN SEA
Figure B
AB
CI
UDMZ
SSZ
ZFTB
PERSIAN GULF
0 300 Km
Elevation [m]
0 - 500
500-1000
1000-1500
1500-2000
2000-2500
2500-3000
3000-3500
3500-5500
N
(b)
47°E
48°E
49°E
50°E
Figure C
CASPIAN SEA
MB
GPB
ZB
QOR
TB
AB
TR
ALB
ZAB
SR
HR
A
B
37°N
36°N
Elevation [m]
3092
-36
0 30 Km
N
(c)
48°30'E
49°00'E
49°30'E
37°30'N
37°00'N
CASPIAN SEA
Rasht
Manjil
Zanjan
39.7±1.3
38.3±0.9
10.7±0.4
36.7±2.8
38.7±1.4
Fig.3a
Fig.3g
Fig.4e
Fig.4f
Fig.3d
Fig.4c
Fig.3b
Fig.3c
Quaternary
Tertiary intrusives
Neogene red beds
Eocene volcanics
Mesozoic clastics and carbonates
Paleozoic undifferentiated
Precambrian basement
Anticline
Syncline
Strike slip fault
Thrust fault
Inferred thrust fault
Unknown kinematic
Name of main cities
0 20 40 Km 80
(d)
SW
Iranian Plateau
Tarom Mt
Tarom Basin
Alborz Mt
NE
Elevation (Km)
3
2
1
0
-1
0
10
20
30
40
50
60
70
80
A
Horizontal Distance (Km)
B
(e)
Late Miocene - Quaternary
Middle - late Miocene
Oligocene? - early Miocene
Middle - late Eocene
Paleocene ? - early Eocene
Cretaceous
Middle-Upper Jurassic
Upper Triassic-Lower Jurassic
Conglomerates and volcanics (up to 1 km)
Upper Red Fm (up to 3 km)
Qom Fm (up to 1 km)
Lower Red Fm (up to 0.3 km)
Karaj Fm (3 to 6.5 km)
Ziarat Fm (up to 0.7 km)
Fajan Fm (up to 0.5 km)
Cretaceous limestones and clastics (up to 1.5 km)
Lar Fm (up to 0.5 km)
Shemshak Fm (up to 2 km)
Arabia-Eurasia continental collision
Neo-Tethys subduction
Collisional deformation
Earliest stage of collisional deformation
Late Cretaceous-Paleocene contractional deformation
Cimmerian Orogeny
Intrusives (pluton, dike, sill)
Tuffaceous sandstone
Tuff and volcanics
Limestone
Shale, mudstone, marl
Sandstone
Conglomerate
Angular unconformity

2. Material and Methods

To unravel the basin-fill history of the intermontane Tarom Basin and its tectono-stratigraphic evolution in the framework of collisional deformation and plateau building processes, we performed a multidisciplinary study including:

1. Field observations and mapping combined (Figures 3 and 4) with a detailed sedimentologic analysis to provide the basis for an assessment of the depositional environments and their spatiotemporal evolution (Sections 3.1 and 3.2; Figures 5 and 6)
2. A geochronologic study (zircon U-Pb dating) of the uppermost volcanic rocks of the Karaj Formation and the overlying red beds to obtain independent age constraints (Section 3.3; Figure 7)
3. A paleomagnetic analyses (Figure 8) for magnetostratigraphic dating to provide a chronostratigraphic framework for the late Cenozoic basin-fill sediments (Section 3.4; Figures 9–11)
4. A provenance study (sandstone petrography and paleocurrent analysis; Section 3.5), to identify compositional variations related to the exposure of new sediment sources and/or drainage-pattern reorganizations in the sediment source area (Figure 12)

This multidisciplinary approach was employed on two stratigraphic sections exposed along the southern margin of the basin (TV and KA sections; Figure 2) and on a third one located in the northern limb of a north-vergent anticline in the central sectors of the basin (GH section; Figure 2). The red beds exposed along the southern basin margin are tilted northward with a dip angle of 14°–30°, whereas in the central sectors of the basin they are steeply dipping to the north (and occasionally overturned) with a dip angle of 40°–88°. These sections are stratigraphically continuous and are not affected by major faults, therefore they represent an ideal setting for magnetostratigraphic sampling. In the following, we provide a brief description of the employed methods.

2.1. Depositional Systems

Based on our field observations (lithological characteristics, lateral and vertical grain size variations, sedimentary structures and geometry of the sedimentary bodies) and according to the classification scheme of Miall (1985, 1996), we established a total of 18 lithofacies types (Figure 5; Table SI1-1) and recognized eight facies associations (Figure 6). The combination of the facies associations led to the reconstruction of four depositional environments (alluvial fan, braided river, playa-lake and lacustrine settings; Figure 7; Table SI1-2).

2.2. Zircon U-Pb-Dating

Five samples were collected in the Eocene volcanic rocks and the Neogene red beds. Mineral separation was performed according to standard techniques (crushing, sieving, water table, magnetic separation and heavy liquids as needed) at the Institute of Earth and Environmental Science of the University of Potsdam. Zircons grains where sent to the Geochronology Laboratory in the Department of Earth and Space Sciences, University of California Los Angeles for the sample preparation and the laboratory measurements. Crystals were examined using a high magnification binocular microscope. Rounded zircons were avoided, and only transparent, fracture-free and euhedral crystals were hand-picked. Crystals are characteristically euhedral

Figure 1. (a) Shuttle Radar Topographic Mission Digital Elevation Model (SRTM DEM) of Iran showing the IP; the white polygons indicate the main drainage basins forming the IP while the black line shows the approximate location of the suture zone, which separates the lower Arabian plate (and the Zagros Fold and Thrust Belt; ZFTB) from the upper Eurasian plate (Ballato et al., 2017). The Urumieh Doktar Magmatic Zone (UDMZ) and the Sanandaj Sirjan Zone (SSZ) represent the backbones and the margins of the plateau, respectively. (b) DEM of NW Iran. Abbreviations: Tarom Basin (TB), Mianeh Basin (MB), Alamut Basin (ALB), Great Pari Basin (GPB), Zanjan Basin (ZB), Zarin Abad Basin (ZAB), Tarom range (TR), Alborz Mountains (AB), Sultanieh range (SR), and Halab range (HR). Note the QOR drainage system (~55,000 km^2) that connects the IP and the Caspian Sea through the Tarom Basin. A′–B′ line shows the approximate location of the crustal scale section shown in Figure 15c. The white dash line shows the margin of the plateau during internal drainage condition until ~4 Ma, when the QOR was established (Heidarzadeh et al., 2017). (c) Simplified geologic map of NW Iran (R. G. Davies, 1977; Stocklin & Eftekharnezhad, 1969) showing the location of the panoramic field photographs of Figure 4. The red stars (and black ages) show the location of our new zircon U-Pb ages (expressed in Ma); the black stars (and blue ages) represent reworked Eocene volcanic material within red beds that do not provide information on their depositional age (Table 1). (d) Regional geological cross section (modified after Stocklin et. al, 1969). (e) Simplified MesoCenozoic tectono-stratigraphic scheme of NW Iran. (e) Simplified tectono-stratigraphic evolution of the NW Iran including major geodynamic events.

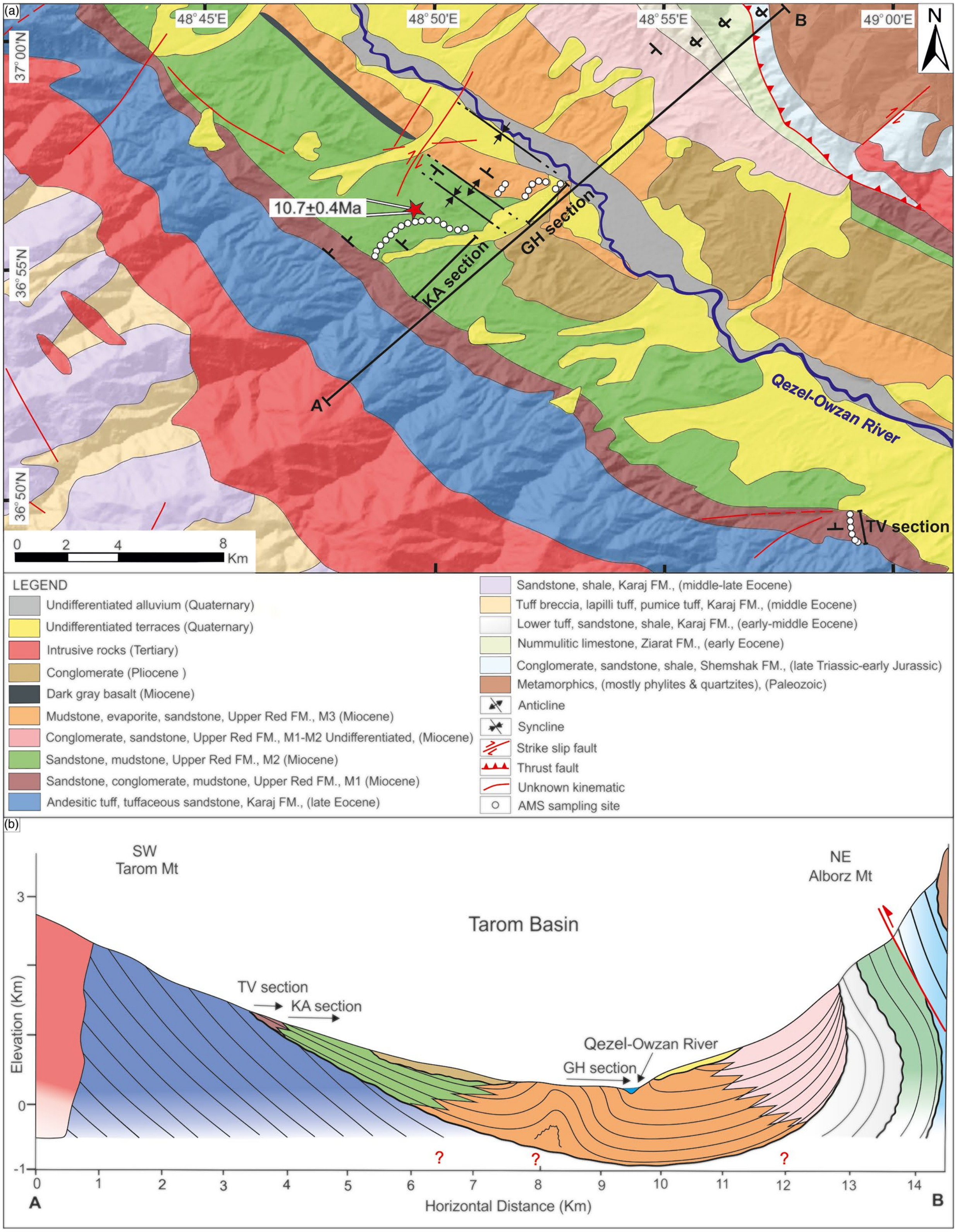

Figure 2. (a) Geologic map (Amini, 1969) superimposed on a SRTM hillshade model of the study area (TB). The white circles show the position of some magnetostratigraphic samples and delineate the location of the three investigated stratigraphic sections named TV, KA, and GH (see also black lines). The base of section GH is also visible in Figure 4g, while a typical outcrop of section TV is shown in Figure 4d. (b) Geologic cross section across the Tarom Basin based on our field data.

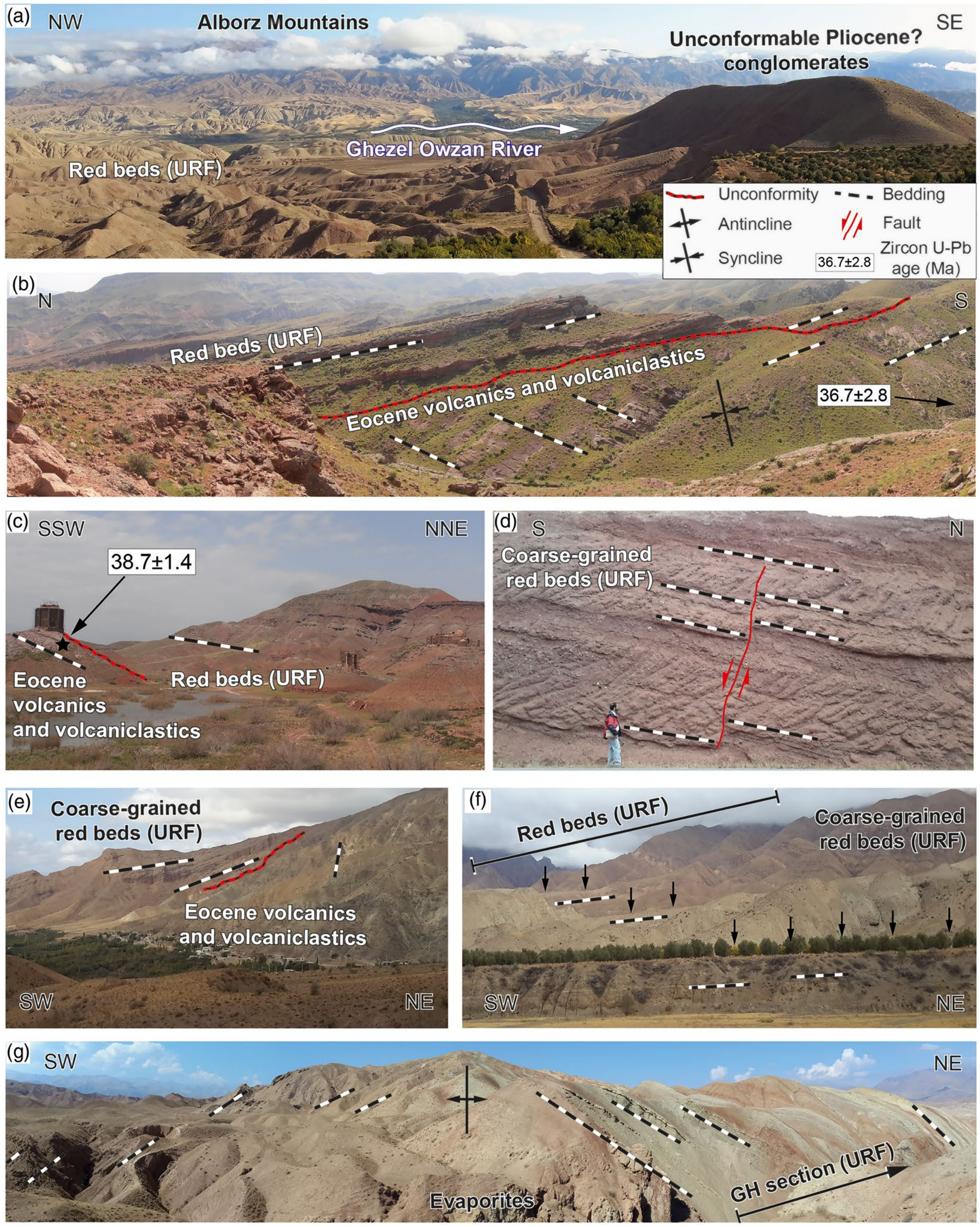

Figure 3. Panoramic field photographs (see Figure 1 for location) highlighting the main geometrical relationships among the units and formations exposed in the Tarom Basin. (a) Northeast-facing photo showing conglomerates of supposed Pliocene age that rest unconformably on deformed red beds; the conglomerates are tilted to the NNE and have a dip angle of ~25°. On the foreground the mountain front of the western Alborz Mountains with several generation of terraces (see figure g for details). (b and c) Southeast- and northwest-facing photos documenting the unconformity between the Karaj Formation and the red beds in the southern margin of the basin. (d) Synsedimentary normal fault exposed along the TV sections (Paknia, 2019; PhD thesis). (e and f) Northwest-facing photos documenting the unconformity between the Karaj Formation and the red beds in the southern margin of the basin. (g) West-facing photo displaying three major terrace conglomerates (see black arrows); these deposits are virtually undeformed and cover in unconformity steeply dipping red beds. (h) Northwest-facing photo showing the core of an intrabasinal anticline that represents the base of the stratigraphic section GH.

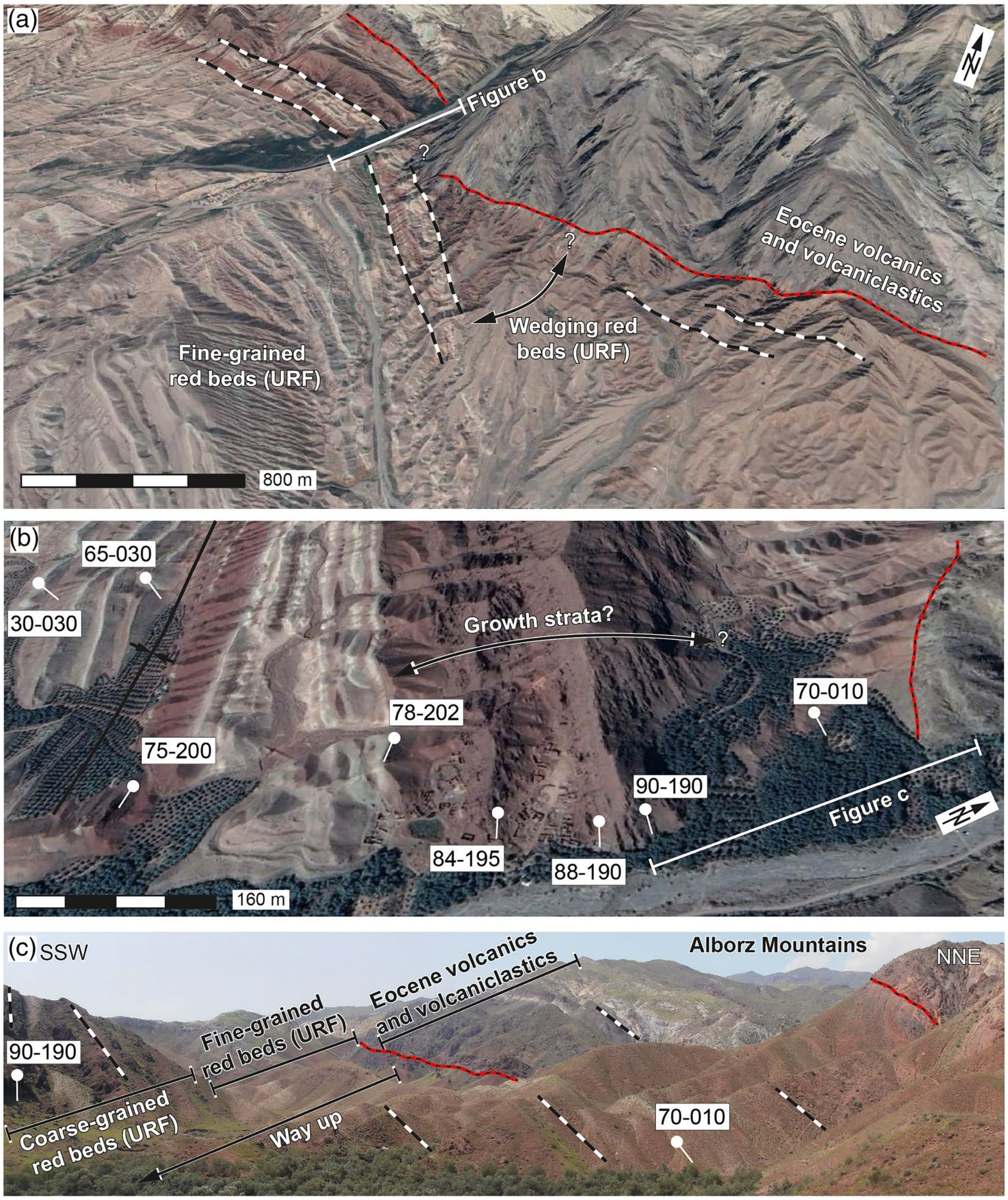

Figure 4. (a and b) Prospective Google Earth satellite imageries, and (c) field photo of the growth strata observed near the base of the red beds along the northern margin of the Tarom Basin (see Figure 3 for legend). The bedding is reported in the white boxes as dip angle—dip direction. Note the wedging geometry of the red beds in Figure 1a corresponding to the rapid shallowing upward trend of the dip angles shown in Figure 1b. Note also the irregularity of the angular unconformity between the red beds and the underlying volcanic rocks of the Karaj Formation, possibly reflecting the existence a paleo-topography.

and doubly terminated with generally long prismatic stems. The dimensions of the analyzed zircon crystals typically range from 100 to 450 and 40–140 μm in length and width, respectively, corresponding to elongation ratios between 2.5 and 3.5. The exception is represented by sample GH-15-03 that yielded few and much smaller zircons. The selected grains were mounted in epoxy, polished and coated. Carbon coated mounts were used for cathodoluminescence imaging using a Tescan Vega-3 XMU variable-pressure SEM at UCLA. Cathodoluminescence textures show narrowly spaced and often uninterrupted oscillatory zoning (Figure SI2-1). Zircon inherited cores were few and only rim domains were targeted in the isotopic analyses (Figure SI2-1). Mounts were then coated with ~100Å of Au. U-Pb ages were determined based on U, Pb,

10.1029/2020TC006254

Figure 5. Close up view photographs of lithofacies characteristics. (a) Disorganized, structureless, matrix-supported, mostly monomictic conglomerate (clasts are Eocene volcanic rocks) with subangular to angular clasts reflecting mass flow deposits. (b) Disorganized, structureless, clast-supported, mostly monomictic conglomerate with crude bedding and subangular to moderately rounded clasts (stream-flood deposits). (c) Conglomerates and coarse-grained sandstones with planar cross bedding representing traction current bedforms. (d) Horizontally laminated sandstone and rippled sandstone indicating traction currents of variable energy in sandy dominated system. (e) Lenticular bedding with symmetrical rippled sandstone alternated with laminated mudstone reflecting an alternation of current (bidirectional) and suspension deposits. (f) Massive structureless to finely laminated calcareous mudstone (suspension deposits). (g) Mudstone with carbonate nodules indicating paleosol formation. (h) Evaporate deposits reflecting evaporation from standing water.

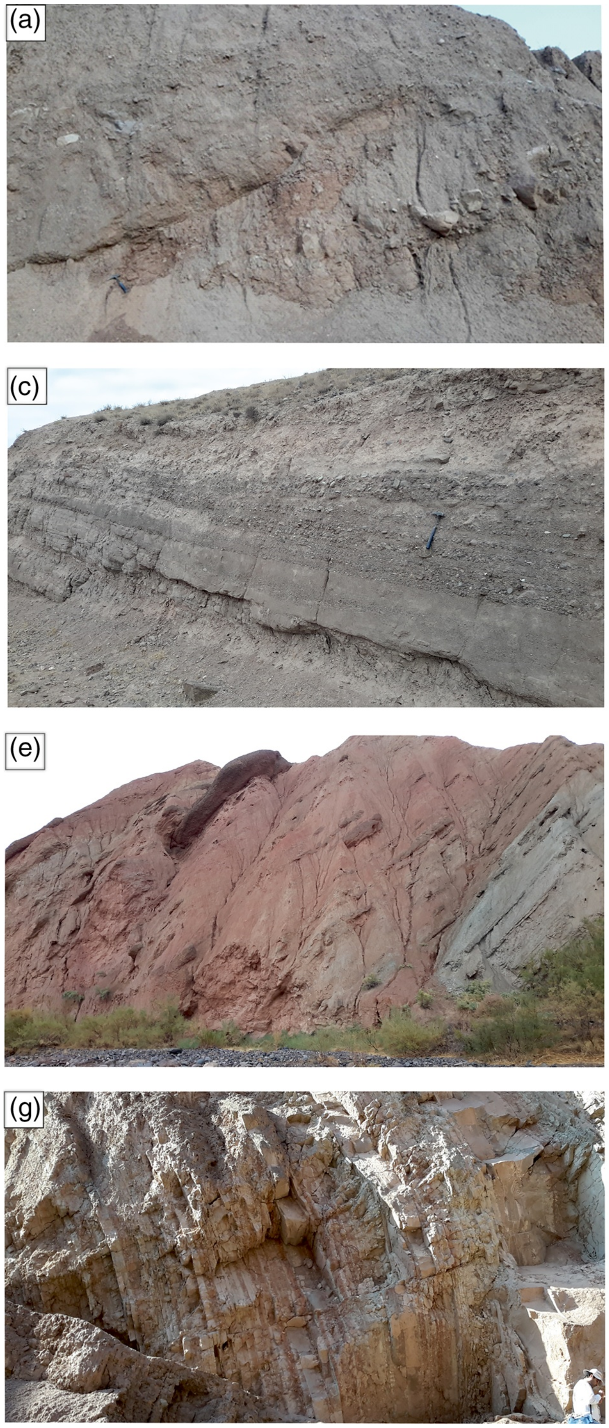

Figure 6. Representative views of different depositional systems in the Tarom Basin. (a) Disorganized granule-boulder conglomerate (facies association G1; base of KA stratigraphic section) and (b) moderately to well organized granule-boulder conglomerate (facies association G2; KA stratigraphic section) representing an alluvial fan setting. (c) Horizontally to trough cross-stratified pebbly sandstone and conglomerate in a fluvial channel (facies association S; KA stratigraphic section), of a braided river system. (d) Horizontally, thin bedded, fine grained sandstone, and laminated mudstone sheets (facies associations SM; KA stratigraphic section) representing flood plain deposits of the braided river system. (e) Overview of the braided river system with lenses of conglomerate and coarse-grained sandstone (facies association S and G3) embedded in flood plain deposits (facies associations SM; top of GH stratigraphic section). (f) Fine grained sandstone and mudstone deposits with flat geometry (facies association SM; GH stratigraphic section) reflecting deposition in the shoreface-offshore transition in a lacustrine depositional setting; the sandstone layers indicate distal storm beds. (g) Alternation of mudstone and fine-grained sandstone deposit with flat to tabular geometry (facies association SM; base of GH stratigraphic section; lacustrine depositional setting); when the mudstone dominates deposition occurred in the offshore setting, otherwise the alternation of mudstone and sandstone indicates deposition in the shoreface-offshore transition. (h) Gypsum layers (evaporite deposits) precipitated during short-lived desiccation episodes (facies association E, GH stratigraphic section), representing a playa lake depositional setting.

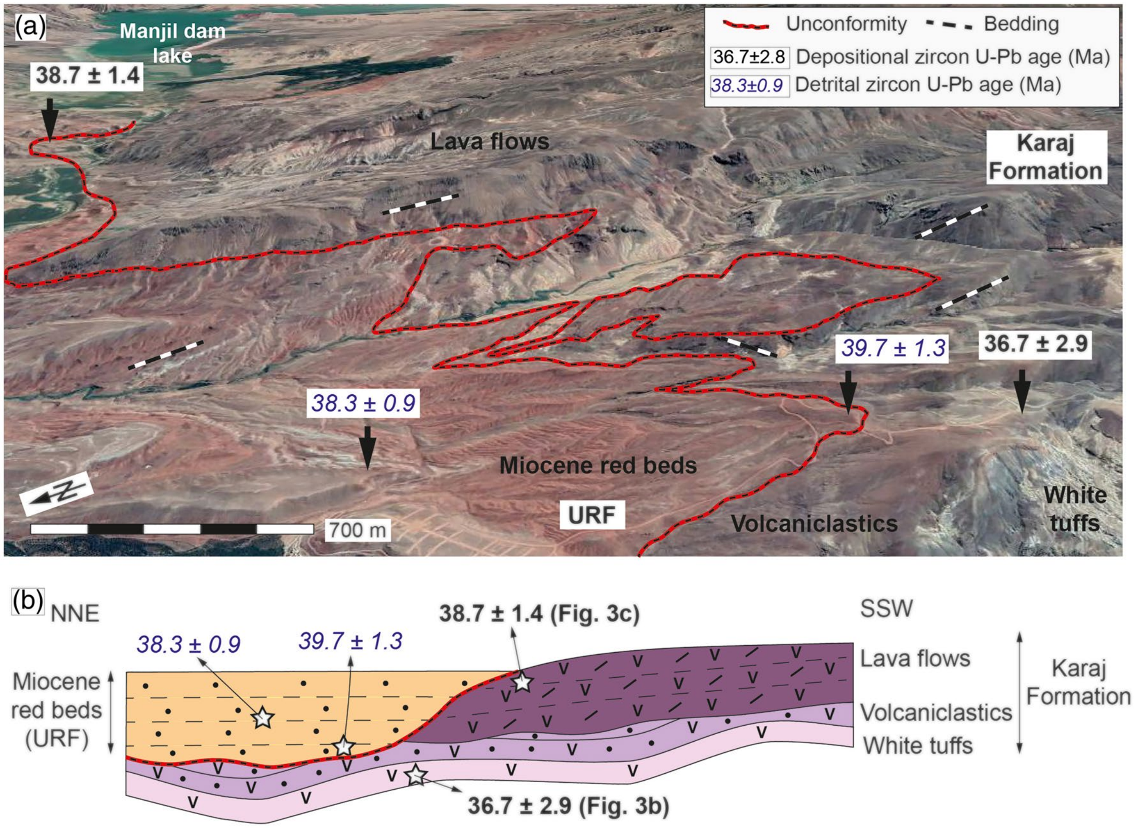

Figure 7. (a) Google Satellite Imagery showing the relationship between the Karaj Formation and the red beds along the southern margin of the basin in proximity of the Manjil dam lake (see the same ages reported in Figure 1 for location). The white dashed line shows the unconformity contact between the Karaj Formation and the Upper Red Formation (URF). (b) Schematic cartoon showing the geometrical relationships between the top of the Karaj Formation and the red beds along the southern margin of the Tarom Basin.

and Th isotopic spot measurements using the UCLA CAMECA ims 1,270 ionprobe following the analytical procedure explained in Schmitt et al. (2003). Each analytical run collected data for 10 cycles, and age calculations were performed by means of ISOPLOT (Ludwig, 2003). The final ages are listed in Table 1 and represent the weighted mean at the 95% confidence level for a given number of ages ranging from four to sixteen (Mahon, 1996; see also Figure SI2-2 in the supporting information).

2.3. Paleomagnetic Analysis

A total of 536 oriented samples (mostly mudstones and few cases very fine to fine grained sandstones) were collected from the three investigated stratigraphic section with a mean sampling interval of typically ~3 m and at least two cores at each site. In case of poor outcrop conditions or in sectors composed mostly of coarse-grained sediments the sampling intervals was as large as ~5–6 m. Paleomagnetic sampling was carried out using an ASC 280E petrol-powered transportable drill with a water-cooled diamond bit. The orientations of the cores were measured by using a magnetic compass to determine both azimuth of core axis (declination) and dip of the core axis (inclination) and also corrected for ~5°E present day declination using magnetic field calculators (www.ngdc.noaa). Seventy-two samples were collected along the 153-m-thick TV stratigraphic section (M1 member), while 143 and 321 samples were collected from the 565-m-thick KA (M2 member) and the 1,185-m-thick GH Section (M3 member), respectively.

Magnetic measurements were then performed using a 2-G Enterprises superconducting rock magnetometer equipped with DC-SQUID coils within a magnetically shielded room at the Alpine Laboratory of Paleomagnetism (ALP) at Peveragno (Turin) and at the INGV Laboratory of Paleomagnetism (Rome, Italy) shielded room in Rome, both in Italy. After measuring the normal remanent magnetization (NRM), samples were

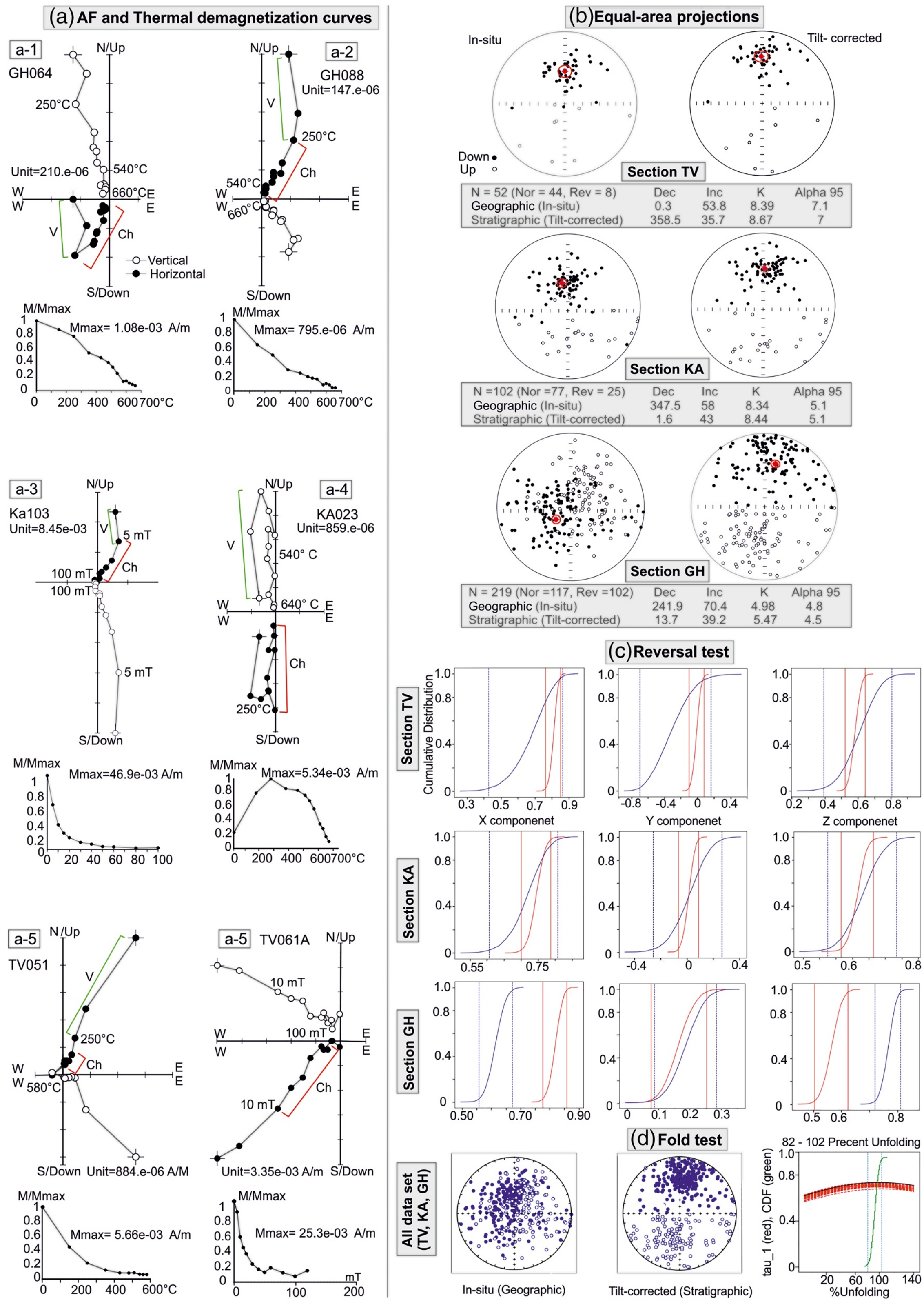
(a) AF and Thermal demagnetization curves
a-1 GH064 Unit=210.e-06 250°C 540°C 660°C
a-2 GH088 Unit=147.e-06 250°C 540°C 660°C
Mmax= 1.08e-03 A/m
Mmax= 795.e-06 A/m
a-3 Ka103 Unit=8.45e-03 5 mT 100 mT
Mmax=46.9e-03 A/m
a-4 KA023 Unit=859.e-06 540° C 640° C 250°C
Mmax=5.34e-03 A/m
a-5 TV051 250°C 580°C Unit=884.e-06 A/M
Mmax= 5.66e-03 A/m
a-5 TV061A 10 mT 100 mT Unit=3.35e-03 A/m
Mmax= 25.3e-03 A/m
Vertical
Horizontal
(b) Equal-area projections
In-situ
Tilt- corrected
Section TV
N = 52 (Nor = 44, Rev = 8) Dec Inc K Alpha 95
Geographic (In-situ) 0.3 53.8 8.39 7.1
Stratigraphic (Tilt-corrected) 358.5 35.7 8.67 7
Section KA
N =102 (Nor =77, Rev = 25) Dec Inc K Alpha 95
Geographic (In-situ) 347.5 58 8.34 5.1
Stratigraphic (Tilt-corrected) 1.6 43 8.44 5.1
Section GH
N = 219 (Nor =117, Rev =102) Dec Inc K Alpha 95
Geographic (In-situ) 241.9 70.4 4.98 4.8
Stratigraphic (Tilt-corrected) 13.7 39.2 5.47 4.5
(c) Reversal test
Cumulative Distribution
X componenet
Y componenet
Z componenet
Section TV
Section KA
Section GH
(d) Fold test
All data set (TV, KA, GH)
In-situ (Geographic)
Tilt-corrected (Stratigraphic)
82 - 102 Precent Unfolding
tau_1 (red), CDF (green)
%Unfolding

subjected to stepwise (up to 15 steps) thermal demagnetization, using heating routine increments (150°C up to a temperature of 480°C and 30°C–50°C increments above 480°C) until the signal decreased below the instrumental detection limit or random changes of the paleomagnetic directions occurred (see specific information in the tables of the supporting information). A set of sister specimens were chosen for AF demagnetization. Stepwise alternating field (AF) demagnetizations were done using a three-axis demagnetizer with a maximum field of up to 100/120 mT, coupled with a 2G-DCSQUID magnetometer (see specific information in the tables of the supporting information). This led to the isolation of high-temperature and high-coercivity stable directions. The computation of the characteristic remanent magnetization (ChRM) was obtained through the principal component analysis (Kirschvink, 1980) fitting the linear component of the stable directions, while data statistical analysis was performed using the Fisher statistics (Fisher, 1953). Data processing was conducted by means of the software Remasoft 3.0 (Chadima & Hrouda, 2006). To assess the primary nature of the isolated ChRM directions the reversal and fold tests were performed using a Python script, based on the orientation matrix method of Tauxe and Watson (1994). For each magnetostratigraphic section, the bootstrap reversal test (Tauxe et al., 1991) was carried out separately. Finally, the virtual geomagnetic pole (VGP) for each sample was obtained from the ChRM vectors.

2.4. Sandstone Petrography

Six sandstone samples collected along the KA and GH stratigraphic sections were analyzed under a polarized microscope in transmitted light. Petrographic analyses were performed according to the Gazzi-Dickinson method (Ingersoll et al., 1984) and for each sample, 400 points were counted. Results were plotted on QFL-c, QFL, and Lm-Lv-Ls ternary diagrams (Figures 13a–13c, respectively; Tables SI4-1 and SI4-2; Dickinson et al., 1985; Garzanti, 2019) in order to frame the sediment provenance area into specific tectonic settings.

3. Results

In the following we summarize the main results. The complete data set is shown in form of tables and figures in the supporting information, while the row paleomagnetic data are available at https://data.mendeley.com/datasets/n5z4h9dy6x/2 /DOI:10.17632/n5z4h9dy6x.2 and can be accessed with the free software Remasoft 3.0 (Chadima & Hrouda, 2006).

3.1. Stratigraphic and Structural Setting of the Tarom Basin Based on Our Field Observations

The red beds of the Tarom Basin consist of coarse- to medium-grained clastic deposits passing laterally toward the basin axis to finer grained sediments and evaporites (Figure 3b). The stratigraphic sections along the southern margin (TV and KA sections) cover the lowermost stratigraphic interval of the basin fill and consist mainly of reddish or light brownish conglomerates with intercalations of mudstone and fine-grained sandstone layers evolving up section into channelized sandstones with conglomerate lenses and finer-grained sediments with tabular geometries. The stratigraphic section in the central sectors of the basin (GH section) consists mainly of reddish, greyish, and brownish mudstones, thin bedded sandstones and evaporates layers, locally with intercalations of conglomerates lenses, which become more abundant toward the top of the section. The minimum thickness of the basin-fill sediments observable in the field in the central sectors of the basin is about 1,185 m, while the lack of major intrabasinal unconformities within the red beds suggests that sedimentation was rather continuous. In some parts, the red beds are unconform-

Figure 8. (a) Tilt corrected diagrams of Thermal and AF demagnetization analysis of representative samples. Demagnetization diagrams and intensity decay curves are shown to the left. The black and white circles represent projections onto the horizontal and vertical plane, respectively (Zijderveld, 1967), while numbers at each demagnetization step denote temperatures in °C (150–680) and magnetic field values in mT (5–120). Ch and V abbreviations on demagnetization diagrams represent the ChRM and the viscose components, respectively (b) Mean normal and reverse polarity of ChRM components for the three investigated stratigraphic sections on equal-area stereographic projection in geographic and tilt-corrected coordinates (Dec = declination; Inc. = inclination; K = precision parameter, α_{95} = semi-angle of the cone of 95% confidence). (c) Bootstrap reversal test results for the three stratigraphic sections and (d) fold test results for the entire data set (Tauxe et al., 1991). The reversal test on TV and KA samples is positive, while GH samples show a negative reversal test. The fold test (all samples from the three stratigraphic sections) is positive.

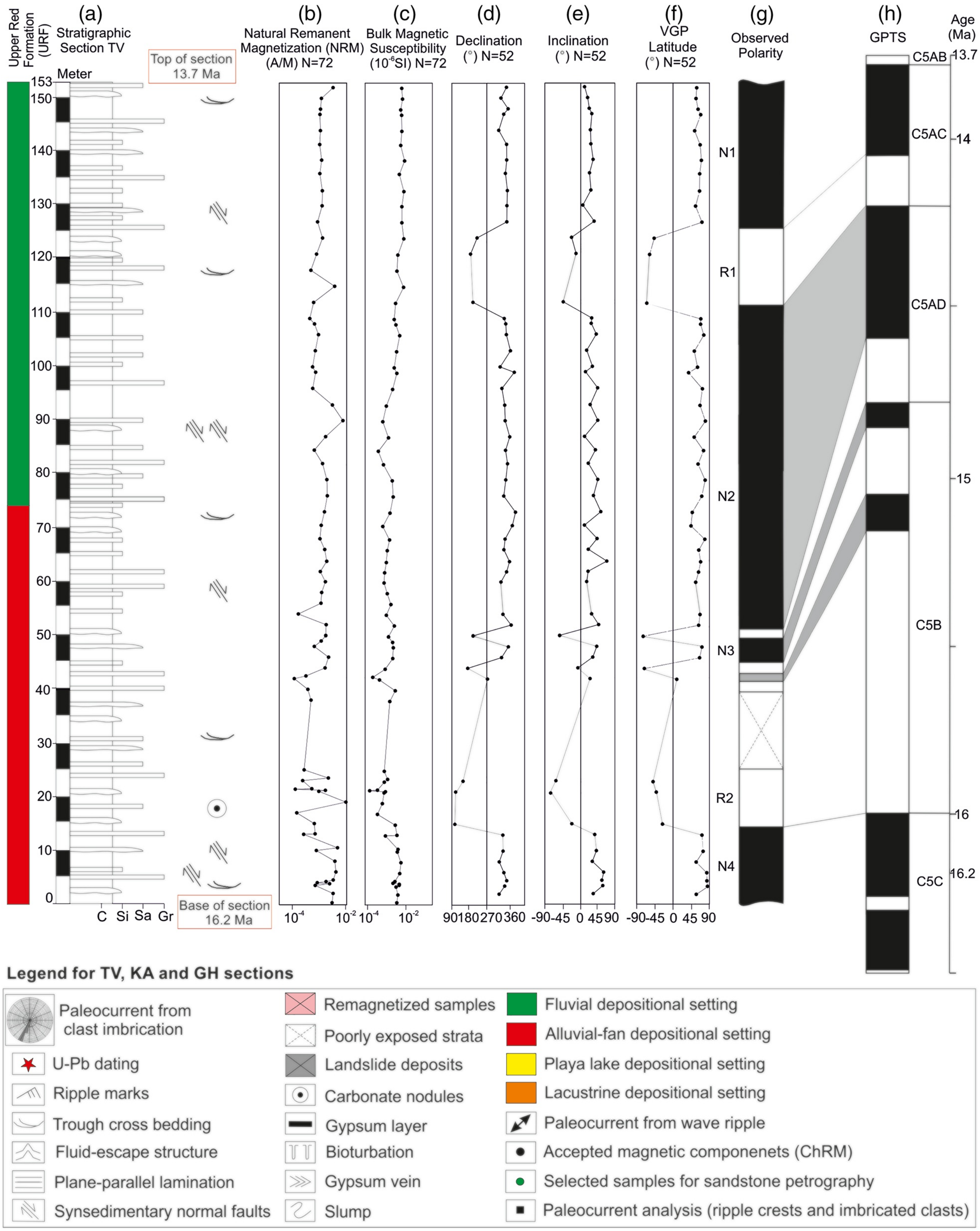

Figure 9. (a) Stratigraphic sections TV including (b) natural remnant magnetization (NRM), (c) Bulk magnetic susceptibility, and (d) Virtual geomagnetic pole latitude (VGP). Note that C, Si, Sa, Gr on the horizontal line of stratigraphic sections mean clay, silt, sandstone and conglomerate, respectively. The VGP latitudes were used for constructing (e) observed polarity scales, which were subsequently correlated each stratigraphic section with (f), the reference GPTS (geomagnetic polarity time scale) of Gradstein et al. (2012). Gray magnetozones of observed polarity scale were detected by means of only one sample.

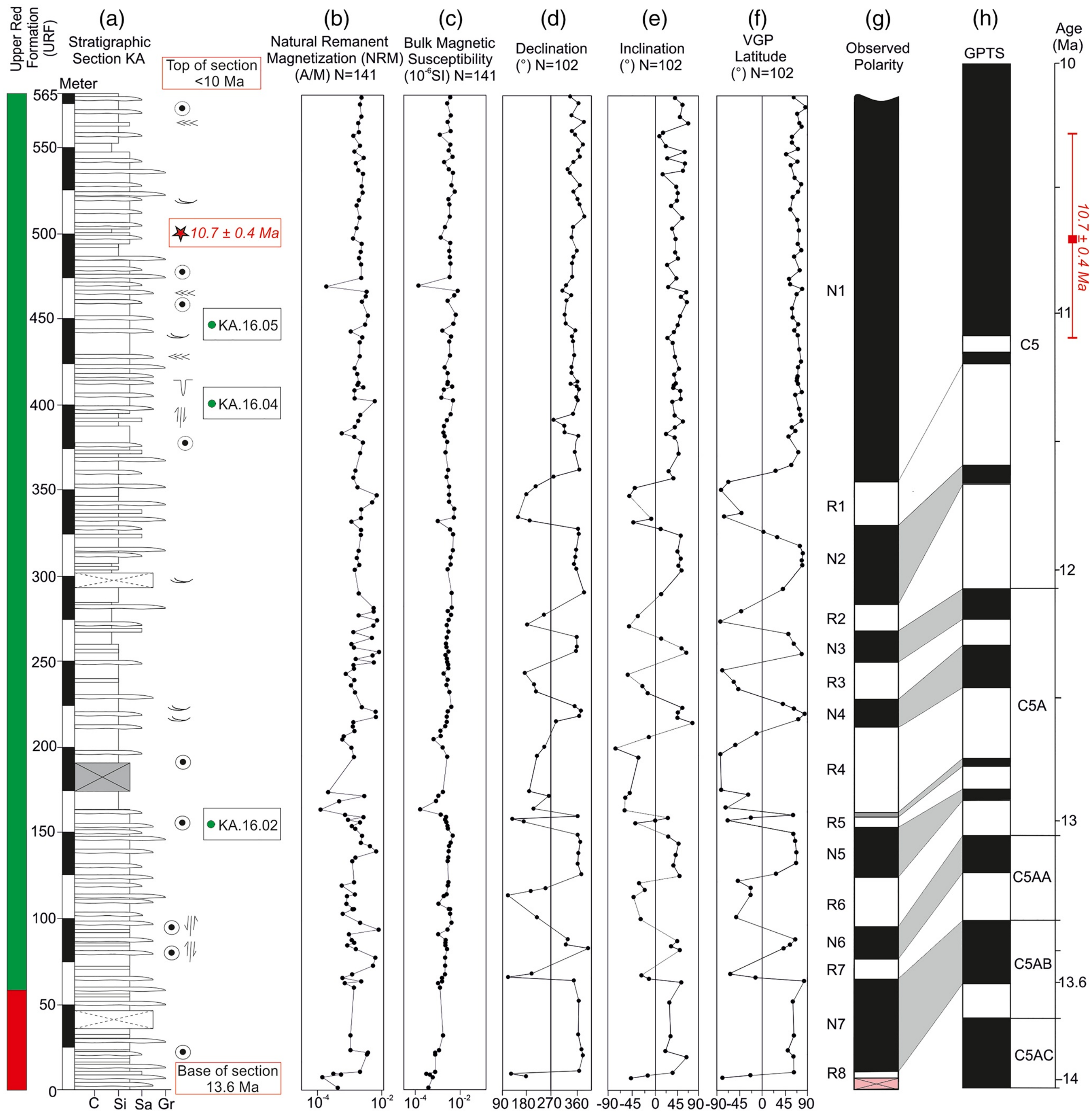

Figure 10. (a) Stratigraphic sections KA including (b) NRM, (c) Bulk magnetic susceptibility, and (d) VGP latitude. The VGP latitudes were used for constructing (e) observed polarity scales, which were subsequently correlated each stratigraphic section with (f), the reference GPTS (geomagnetic polarity time scale) of Gradstein et al. (2012). Gray magnetozones of observed polarity scale were detected by means of only one sample. See Figure 9 for legend.

ably covered by gently deformed, conglomerates of supposed Pliocene age (Figure 3a). These conglomerates form sparse hills and have an eroded top and have a minimum thickness of few tens of meters. Finally, at least three generations of terrace conglomerates can be observed in the field on both margins of the basin, suggesting the occurrence of recent phases of sediment aggradation and fluvial incision (Figure 3g).

Along the southern margin of the basin, the red beds dip a few degrees toward the NE (10°–30°), while the underlying volcanics are generally steeper dipping (Figure 3c) and can be locally folded (Figure 3b). In

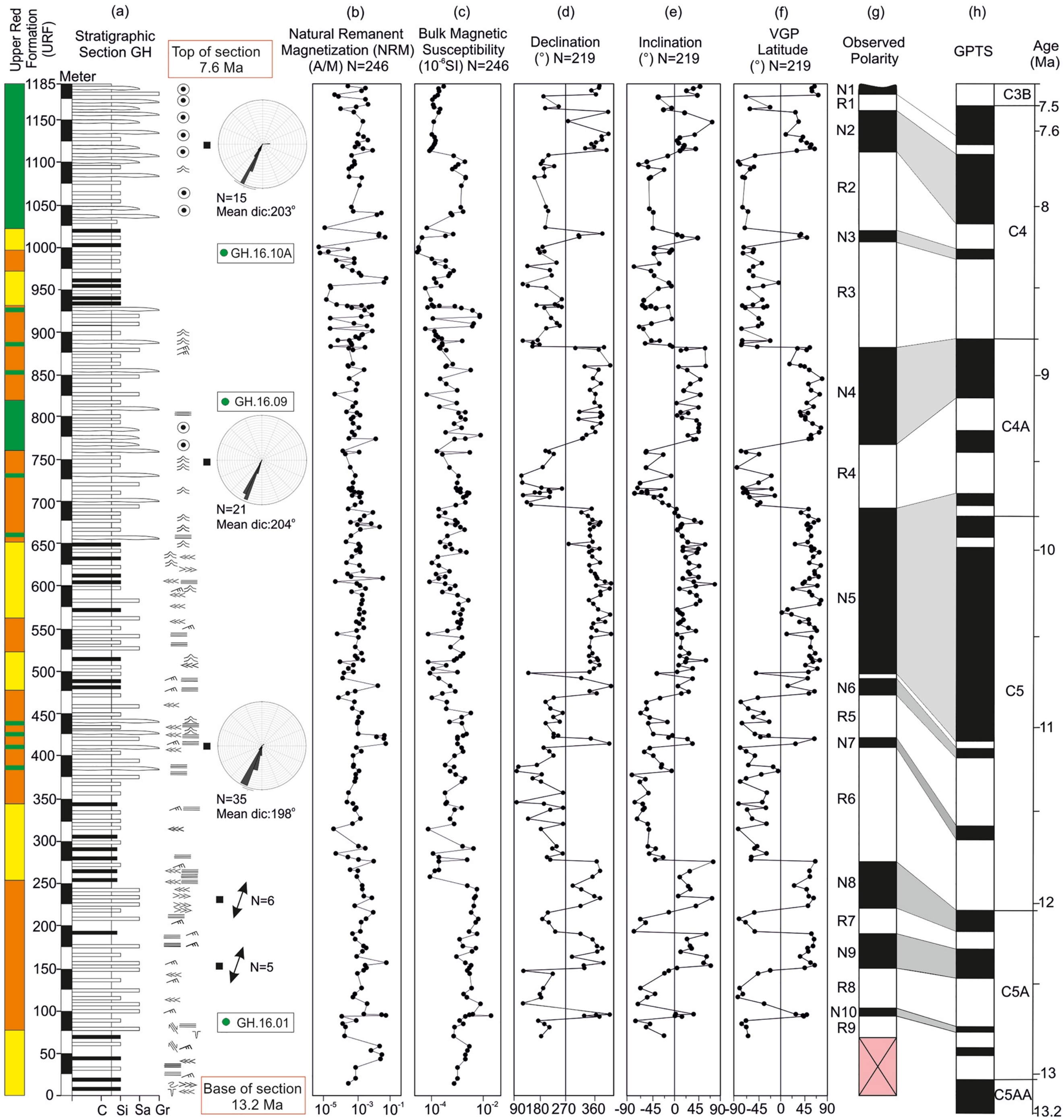

Figure 11. (a) Stratigraphic sections GH including (b) NRM, (c) Bulk magnetic susceptibility, and (d) VGP latitude. The VGP latitudes were used for constructing (e) observed polarity scales, which were subsequently correlated each stratigraphic section with (f), the reference GPTS (geomagnetic polarity time scale) of Gradstein et al. (2012). Gray magnetozones of observed polarity scale were detected by means of only one sample. See Figure 9 for legend.

addition, the southern margin of the basin is characterized by several subvertical synsedimentary normal faults (Figure 3d), mostly parallel to the strike of the basin, that provide evidences for localized extension subparallel to the regional shortening direction (NE-SW; Madanipour et al., 2017). These faults are not linked to major extensional events and hence did not control the basin-scale subsidence pattern (Paknia, 2019; PhD thesis).

Table 1
Zircon U-Pb Dating Results (Note That Sample GH-15-02 was Subsequently Resampled as GH-17-02)

Sample code	Age (Ma)	Error 2s (Ma)	N of grains analyzed	N of grains used	MSWD	Rock type	Formation/Unit	Lat (Dec°)	Long (Dec°)	Elevation (m)
GH-15-01	38.7	1.8	11	10	0.4	Rhyolite	Karaj F	36.74525	49.23086	375
GH-15-02/GH-17-02	39.7	1.3	18	16	1.8	Reworked tuff	Red beds	36.70804	49.14391	752
GH-15-03	36.7	2.8	6	4	0.8	White tuff	Karaj F	36.70342	49.14172	840
GH-17-04	38.3	0.9	10	10	1.0	Tuffaceous sandstone	Red beds	36.72139	49.14806	576
TM-16-01	10.7	0.4	24	13	1.3	Volcanic ash	Red beds	36.91298	48.83748	600
TM-16-01 alternative	11.3.	0.5	24	22	3.8	Volcanic ash	Red beds	36.91298	48.83748	600

Along the northern side of the basin, the setting is more variable and complex, and the Eocene deposits of the Karaj Formation are either subvertical or overturned. In the central-southern sectors of the basin, the unconformable red beds are also subvertical to overturned (Figure 3e) and exhibit a rapid shallowing upward trend and an along-strike strike wedging geometry that suggests the occurrence of growth strata (Figure 4). Conversely, in the central-northern sectors of the basin the angular unconformity is more pronounced, and the red beds dip less than 30° to the south-west, while the underlying Eocene rocks are 30°–40° steeper (Figure 3f). There, we do not have evidence for syndepositional contractional deformation.

The central sectors of the basin are also characterized by several upright syncline-anticlines pairs, subparallel to the strike of the basin with a lateral extent of few kilometers (Figure 2). Figure 3g shows the core of one of these anticlines which is characterized by evaporites layers that have been deformed in a disharmonic manner and may have acted as a local decollement horizon.

Currently, the basin is drained by the ∼800 km long QOR, which is flowing from the elevated IP to the Caspian Sea (Figure 1). The connection between the interior of the IP, the Tarom Basin, and the Caspian Sea occurs through a series narrow bedrock gorges suggesting a protracted history of internal drainage conditions followed by fluvial captures (Heidarzadeh et al., 2017). In particular, the connectivity between the Tarom Basin and the IP must have been established during the last 4 Ma through lake overspill as suggested by the stratigraphic record of a sedimentary basin in the plateau interior (Mianeh Basin, Figure 1b; Heidarzadeh et al., 2017).

3.2. Depositional Systems

3.2.1. Alluvial Fan System

Alluvial fan deposits (Figures 6a and 6b) are located along both margins of the Tarom Basin and include two facies associations: (1) disorganized granule-boulder conglomerate (G1; Figures 5a and 6a) and (2) moderately to well organized granule-boulder conglomerate (G2; Figures 5b and 6b). We interpret the G1 facies association with weakly developed clast imbrications and erosive basal contacts as high-energy stream-floods equivalent to those produced by gravel-laden streams or sediment gravity flow deposits (hyperconcentrated and turbulent flow) in poorly confined channels (Figures 5a and 6a; e.g., Blair, 1999; Maizels, 1989; Miall, 1996; Ridgway & DeCelles, 1993; Stanistreet & McCarthy, 1993). The beds geometry suggests the occurrence of sheet flows (Hein, 1982) with limited development of longitudinal bars (Boothroyd & Ashley, 1975; Todd, 1989). The G2 facies association is interpreted as traction-current deposits in poorly confined channels under conditions of higher bed shear stress (Figures 5b and 6b; e.g., Ballato et al., 2011; Blair, 1999; Miall, 1996; Stanistreet & McCarthy, 1993).

3.2.2. Braided Fluvial System

The braided river deposits (Figures 6c, 6d, and 5e) are characterized by four facies associations: (1) well-organized granule-pebble conglomerate (G3), (2) sandstone (S), (3) interbedded fine-grained sandstone and mudstone (SM), and (4) evaporite (E). The G3 facies association is interpreted to reflect traction-current

10.1029/2020TC006254

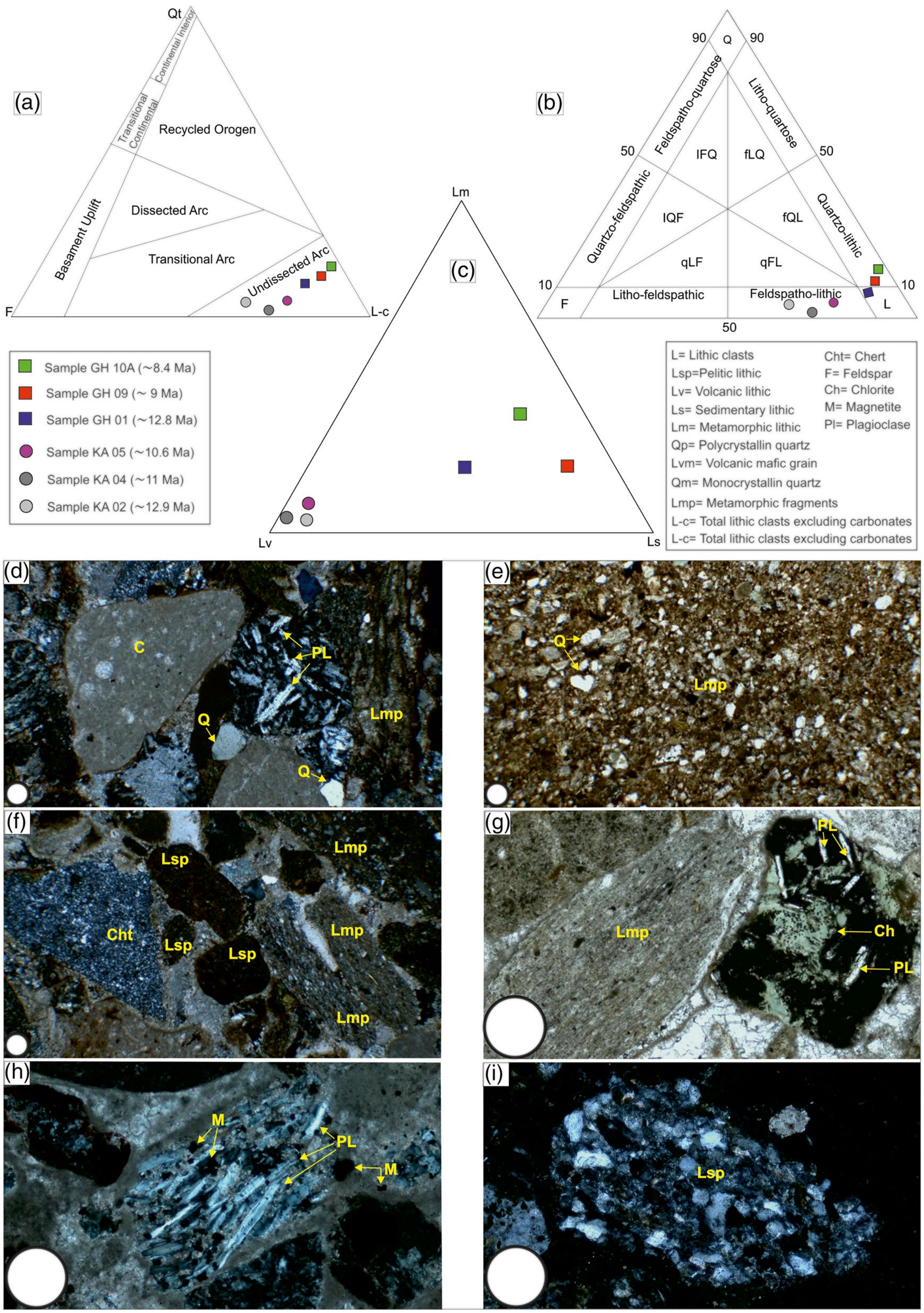

deposits (longitudinal bars or lag deposits) related to the waning stage of high-energy flow in a laterally confined system (e.g., Blair, 1999; Miall, 1996; Stanistreet & McCarthy, 1993). The erosive basal contact, together with the lens geometry and the interfingering with stratified sandstones suggests deposition in a braided channel with a variable proportion of gravel and sand (Figures 5c and 6c; e.g., Miall, 1996). The S facies association is interpreted to represent deposition in lower and upper plane-bed flow regimes in a confined flow (e.g., Miall, 1996). Planar (Sp) and trough cross-stratified, medium to coarse-grained, pebbly sandstones are interpreted as migrating bedforms (fluvial dunes) in a confined flow in an upper to lower flow regime (Figure 5c; Siks & Horton, 2011; Uba et al, 2005). Overall, these observations indicate deposition in a fluvial channel. The SM facies association (Figure 6d) includes sandstones with cross (Figure 5d) and planar lamination (Figure 6d) that are interpreted as sheet-flow deposits in a poorly confined to unconfined flow evolving from the upper flow regime to a waning flow stage. The SM facies association includes also massive to parallel laminated mudstones, which can be locally dominant and are interpreted to represent suspension fallout deposits (e.g., Ghibaudo, 1992) from standing or slowly moving waters in the floodplain (e.g., Miall, 1977, 1978). Locally, the SM facies association are characterized by the development of carbonate nodules and rizholithes indicating paleosols formation (Figure 5g) during lengthy pauses in sedimentation or slow sedimentation rates (e.g., Kraus, 1999). The occasional occurrence of E facies association (Figure 5h) is interpreted to represent precipitation of salt minerals from concentrated water solution after evaporation of standing water in the floodplain. Complete desiccation of standing water is also documented by mud cracks (e.g., Lowenstein & Hardie, 1985).

Finally, in the KA stratigraphic section in proximity of the southwestern basin margin we found, embedded in the fluvial deposits, the BD facies association. This disorganized package of blocks with different size and sediments of variable grain size is interpreted as landslide deposits (sturzstrom) caused by gravitational collapse of the adjacent, southern mountain front (e.g., Hermanns & Strecker 1999; Paknia, 2019; PhD thesis). This interpretation is further supported by the occurrence of a clay-reach sheared basal contact and the presence of a dense and irregular network of fractures (jigsaw cracks).

3.2.3. Lacustrine System

The lacustrine system is located along the central sectors of the basin (Figures 5e, 5f, and 6f; section GH) and is characterized by two facies associations: (1) mudstone (M) and (2) interbedded fine-grained sandstone and mudstone (SM). Tabular bodies of laminated mudstone of the M facies association are typical of suspension deposits in a lacustrine offshore setting and indicate a deepening of the system (Figure 5f). Lenses of fine grained-sandstone with symmetrical ripple marks interbedded with mudstone (lenticular and waving bedding Figures 5e and 6f) in the SM facies association indicate deposition in the lacustrine shoreface-offshore transition. In few sectors of the GH stratigraphic section, the tabular sandstones with symmetric ripples become dominant suggesting sedimentation in the lacustrine shoreface (e.g., Chakraborty & Sarkar, 2005; Horton & Schmitt, 1996; llgar & Nemec, 2005; Keighley, 2008). These intervals, however, are relatively rare and generally have a limited thickness (<1 m), therefore most of the lacustrine sediments exposed in the section were deposited either in the offshore or in the shoreface-offshore transition setting.

3.2.4. Playa Lake System

The playa lake system is also located in the central sectors of the basin where it alternates with the lacustrine setting (GH stratigraphic section, Figures 5h and 6h). These deposits include two facies associations such as (1) mudstone (M) and (2) evaporite salt minerals (E). The first facies association (mud-

Figure 12. QFL triangular diagrams with tectonic zones defined by (a) Dickinson (1985) and (b) Garzanti (2019). Q represents total quartz grains (Qm and Qp), F represents total feldspar grains (P and K-feldspars), L and L-c (c) Lm-Lv-Ls ternary plot for the Tarom Basin (Lm; Lvand Ls). (d–i) Representative photomicrographs of sandstone samples. (d) Sample GH-16-05 (stratigraphic position of ~410 m) showing a large calcareous grain (c), a Lvm with PL, a slate fragment with rough cleavage (Lmp) and quartz grains. (e) Sample GH-16-04 (at ~370 m) with metamorphic clasts and Q grains in a terrigenous-carbonatic matrix. (f) Sample GH-16-05 (at ~410 m) with Cht, Lsp, and Lmp (g) Sample GH-16-10B (~990) showing a Lvm with PL altered in green Ch, and Lmp. (h) Sample KA-16-05 (~450) displaying a Lvm with PL and M crystals. (i) Sample GH-16-01 (~ 75 m) showing a Lsp. Note that all photos are under cross polarized light except figure f. Small and large white circles show scales of 4 and 10μ, respectively.

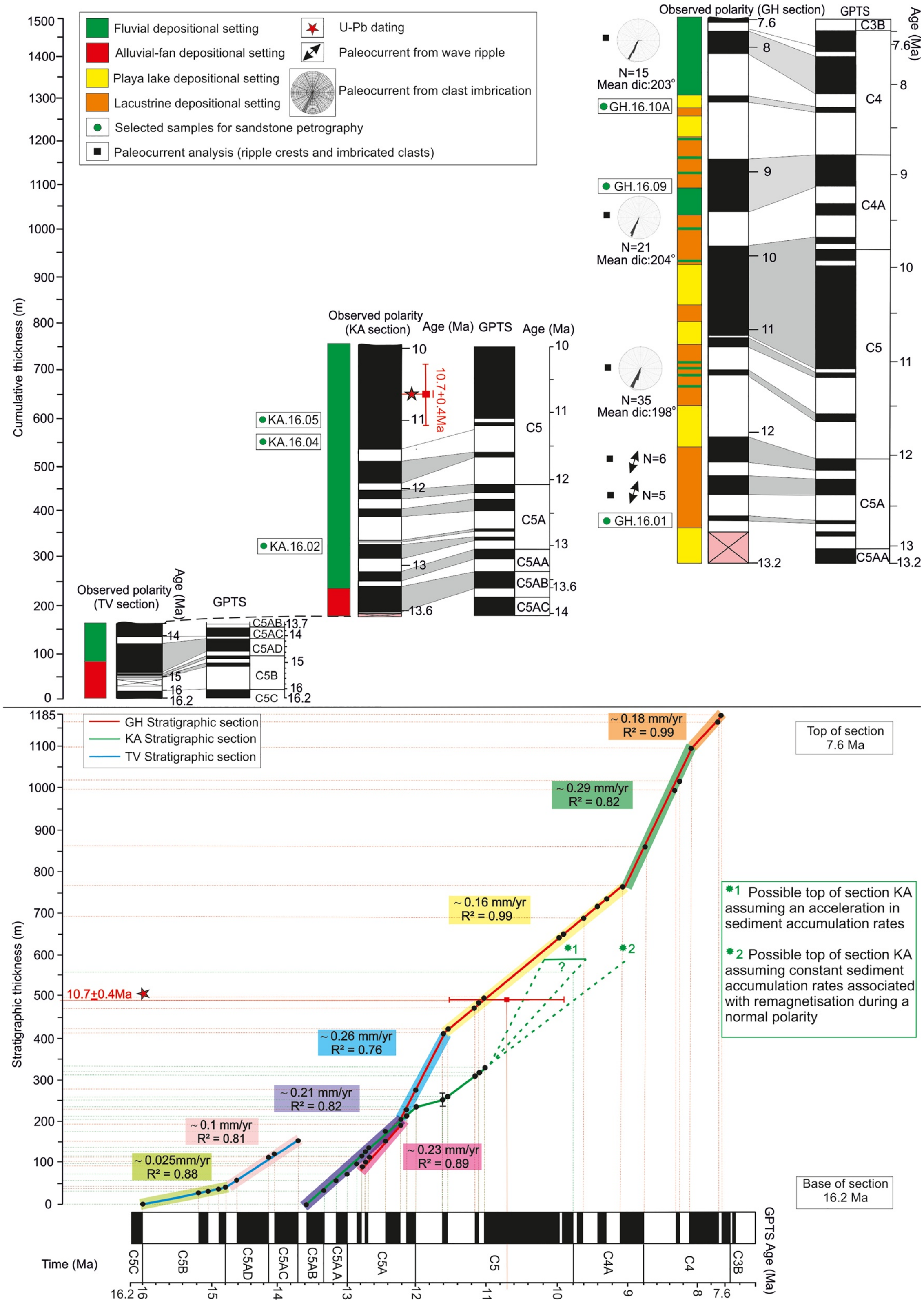

Figure 13. (a) Overview of magnetostratigraphic correlations, distribution of the depositional environments, paleocurrent directions and sample positions for the Tarom Basin. (b) Long-term sediment accumulation rates for the Miocene synorogenic sediments of the three investigated stratigraphic sections. Rates have been obtained by using a linear best fit model (see correlation coefficient R^2) according to the different segments shown with colorful thick lines. The dashed lines allow extrapolating the age of the bottom and top of the stratigraphic sections assuming constant sediment accumulation rates. The star denotes the position of the dated ash layer.

stone; M) is interpreted to represent deposits settled from suspension in arid to semiarid, oxidizing conditions as documented by the presence of red colored sediments and the occurrence of desiccation cracks (e.g., Lowenstein & Hardie, 1985). The second facies association (E) is interpreted to represent evaporite layers (mostly gypsum) precipitated during short-lived rain episodes followed by desiccation (e.g., Lowenstein & Hardie, 1985). Overall, these observations suggest that sedimentation occurred in a shallow playa lake setting.

3.3. Zircon U-Pb Geochronology

Five samples were collected for Zircon U-Pb dating from the Eocene volcanic rocks and the Neogene red beds to constrain the top age of the Karaj Formation and provide independent age constrains on the depositional age of the synorogenic red beds. Results are shown in Table 1 and in the supporting information,

The contact between the Karaj Formation and the overlying red beds is well exposed along both margins of the basin. Considering that the northern margin has experienced a greater degree of deformation and erosion (compare Figures 3b and 3c with Figures 3e, 3f, and 4) we sampled the contact along the southern margin of the basin in two different locations (Figure 1). Sample GH-15-03 represents a >20-m-thick white tuff that can be followed along strike for about 5 km. This lithotype is stratigraphically located below a thick package (several tens of meters) of coarse-grained volcaniclastic deposits that are less suitable for zircon U-Pb dating and represent the top of the Karaj Formation in this area (Figure 3b). These units are characterized by a system of open syncline-anticline pairs with a wavelength of several tens of meters (Figures 3b and 7). Our tuff sample (GH-15-03) yielded only few zircon grains with a weighted average age of 36.7 ± 2.6 Ma (Table 1). We collected another sample (GH-15-01) along strike to the SE from a rhyolite exposed on top the Karaj Formation (Figure 3c). In this area the angular unconformity with the overlaying red beds has a low angle (<10°). This sample yielded a weighted average age of 38.7 ± 1.4 Ma. This age overlaps with the previous sample (within a two-sigma error) suggesting that the termination of widespread arc volcanism in NW Iran should have occurred sometime between 38 and 36 Ma. This age agrees with those obtained by previous studies (~36 Ma, Ballato et al., 2011; ~37 Ma, Verdel et al., 2011) in central and northern Iran.

An additional, few cm-thick, ash layer (TM-16-01) was collected within the red beds in proximity of the top of the KA stratigraphic section. This sample is fundamental for pinpointing the magnetostratigraphic correlation (see next sections) and yielded a weighted average age over 13 grains of 10.7 ± 0.4 Ma (Table 1). This value does not include nine grains that clustered around 13-12 Ma. If we include these grains the weighted average age over 22 grains will be slightly older 11.3 ± 0.5 Ma (Table 1). These two ages fall within the error, however considering that a ~10.7 My-old (±0.2-0.3 Ma) tuff has been dated about 120 km to the NW in three different locations (Ballato et al., 2017), in the following we will use only the 10.7 Ma age. Accordingly, the 13-12-My-old zircon grains should represent crystals that spent 1–2 million of years in the magmatic chamber before the eruption.

Finally, two more samples were collected in the red beds, directly upsection of sample GH-15-03. These two samples are located right above the unconformity (GH-15-02, resampled in a second stage as GH-17-02) and about 400 m (stratigraphically) above it (GH-17-04; Figure 7). The first sample is a weathered, reworked white tuff, while the second one is a light green tuffaceous sandstone with very pristine biotite crystals. These samples gave very similar ages (39.7 ± 1.3 and 38.3 ± 0.9 Ma, respectively; Table 1), which look almost identical to those obtained for the top of the Karaj Formation. Therefore, based on the stratigraphic separation between them we consider these two samples as reworked volcanic material from the eroding Karaj Formation (Figure 7). This means that these ages do not provide indication about the depositional age of the red beds but only their sediment source area.

3.4. Paleomagnetic Results

3.4.1. TV Stratigraphic Section

In the TV stratigraphic section the natural remnant magnetization (NRM) intensities vary between 8.59×10^{-4} and 1.01×10^{-2} A/M, with the highest values (average of 4.34×10^{-2} A/M) in the alluvial fan deposits at the base of the section (first ~15 m), while bulk susceptibility (k) values range from 170 to 10,970 × 10^{-6} SI (Figure 9). Demagnetization diagrams and intensity decay curves of representative paleomagnetic samples for both thermal and AF demagnetization are shown in Figure 8. Thermal demagnetization data reveal two magnetic components: a low-temperature component removed by heating up to 300°C, which is characterized by exclusively normal polarities and is interpreted to represent an unstable viscous component, and a high-temperature component isolated between 300°C and 580°C. Similarly, AF demagnetization data reveals: a low-coercivity component removed between 0 and 15 mT peak fields most likely reflecting to a viscous overprint, and a high-coercivity component isolated between 15 and 120 mT. Both high-temperature and high-coercivity components decay linearly toward the origin (Figure 8) and hence are interpreted to represent the ChRM. Declinations and inclinations of stable ChRM directions for the TV stratigraphic section are plotted next to the stratigraphic log of Figure 9. Collectively, reliable ChRM directions have been obtained in 52 samples out of 72 analyzed cores, with 8 samples showing a reverse polarity and 44 yielding a normal polarity. The maximum angular deviation (MAD) of the successfully isolated ChRM components is lower than 10° for 50 samples, while for two samples it is slightly higher (11.2° and 14.9°).

3.4.2. KA Stratigraphic Section

In the KA stratigraphic section, NRM intensities vary between 9.91 × 10^{-4} and 1.01 × 10^{-2} A/M, whereas bulk susceptibility (k) values range between 460 and 26,570 × 10^{-6} SI (Figure 10). Likewise, the TV section, two magnetic components were identified by means of both AF and thermal demagnetization. For the thermal demagnetization a low-temperature component was removed by heating up to 250°C/300°C while the high-temperature component was isolated between 300°C and 580°C. In few samples, however, the high-temperature component was isolated between 600°C and 640°C suggesting the presence of an even higher temperature magnetic mineral. AF demagnetization was carried only on few samples and also reveals a similar pattern with a low-coercivity component removed between 0 and 15 mT peak fields, and a high-coercivity component isolated between 15 and 120 mT. The vector diagrams of the high-temperature and high-coercivity components decay toward the origin suggesting that they represent stable ChRM directions (Figure 8). Declination and inclination results of stable ChRM directions are plotted in Figure 10 next to the KA stratigraphic log. Overall, 102 specimens out of 143 core samples yielded reliable ChRM directions, with 25 reverse and 77 normal polarities. The MAD of these magnetic components is lower than 10° in 84 samples and it varies between 10.2° and 14.8° in 18 samples.

3.4.3. GH Stratigraphic Section

NRM intensities for the GH samples are about one order of magnitude lower than the other two sections and vary between 9.89 × 10^{-5} and 1.01 × 10^{-3} A/M (Figure 11). Magnetic susceptibility (k) values are also lower than those recorded in the other sections, and range from 70 to 3,650 × 10^{-6} SI (Figure 11). Like the TV and KA stratigraphic sections, thermal demagnetization data from the GH samples reveal a lower temperature component removed by heating up to 300°C. Instead, the high-temperature components are removed either between 300° and 580°, or at 650°C/680°C (Figure 8). In few cases, an additional high-temperature component was isolated between 600°C and 640°C. AF demagnetization was performed only on few representative samples and document the existence of two magnetic components: a low-coercivity component removed between 0 and 15 mT peak fields and a high-coercivity ChRM isolated between 15 and 120 mT. In some samples, however, it was not possible to isolate any magnetic component between 15 and 120 mT, indicating the presence of even higher coercivity magnetic minerals. In both high-temperature and high-coercivity samples the vector diagrams decayed toward the origin indicating successful isolation of the ChRM (Figure 8). Declinations and inclinations of ChRM directions are plotted in Figure 11 next to the GH stratigraphic log. In total, 219 specimens out of 321 sample cores yielded reliable ChRM directions with 102 reverse and 117 with normal polarities. The MAD of these ChRM directions is lower than <10° in 201 samples and is comprised between 10.1° and 14.8° in 18 samples.

3.4.4. Paleomagnetic Field Tests

The fold test was carried out for all the ChRM directions from the three stratigraphic sections (in total 373 direction) in order to have significant differences in the bedding attitudes. In the TV and KA sections the normal and reverse polarities directions are antipodal and the reversal test is positive (Figure 8h). On the contrary in the GH section the normal and reverse polarities are not antipodal and the bootstrap reversal test is negative, suggesting that data population could be partially affected by a recent magnetic overprint that was not completely removed during stepwise demagnetization (Figure 8h). The mean direction of the entire data set is better grouped after tectonic correction (D = 7.5°; I = 40.0°, k = 6.3, $\alpha_{95\%}$ = 3.2°) rather than before (D = 308.8°, I = 74.2°, K = 4.4, $\alpha_{95\%}$ = 3.9) (Figure 8g). At the same time, the bootstrap fold test (Tauxe et al., 1991) is positive showing that the degree of unfolding to produce the maximum τ_1 is between 86% and 106% (Figure 8i). These results demonstrate that the ChRM directions from the three stratigraphic sections were most likely acquired before folding. Finally, it is worth to note that the mean ChRM direction obtained from the three stratigraphic sections (D = 7.5°; I = 40.0°) is very similar to the one obtained from 14 sites from the same basin (D = 10.2°; I = 40.6°) with a positive reversal and fold tests (Mattei et al., 2017). These data further support the primary origin of the ChRM in the red beds of the Tarom Basin as also demonstrated in other paleomagnetic study carried out in the Neogene red beds of Iran (Ballato et al., 2008, 2017; Cifelli et al., 2015; Mattei et al., 2015, 2017, 2020).

On this basis we are confident that our data allow determining correct polarities (latitude of the VGP) and hence to build up a reliable local magnetic polarity stratigraphy.

3.5. Sandstone Petrography and Sedimentary Paleocurrents

The KA sandstones are rather homogenous and mainly composed of volcanic mafic clasts (Lvm, 50% and 58%) and plagioclase (Pl) grains (Figures 12a, 12c, 12d, 12g, and 12h). These are more abundant in the lower part of the section (30 vs. 19%). A few lithic meta felsic particles (Lmv; 6%–9%) as well as a small amount (less than 5%) of quartz and heavy minerals (epidote) are the other constituents observed in the KA samples. Finally, a minor amount (≤3%) of lithic fragments such as lithic volcanic felsic (Lvf), lithic limestone (Lcc), lithic terrigenous (Lp), lithic metasedimentary (Lms) and metabasalt lithic fragment (Lmb) were also observed. Conversely, the GH sandstone samples contain a lower proportion of volcanic lithics, and a higher proportion of low-grade metamorphic particles (Figures 12b, 12c, 12e, and 12f).

The most abundant constituent of the framework components is represented by lithic metasedimentary (Lms) clasts, which range upsection from 14% to 37% (Table 1). The second most abundant constituents are lithic terrigenous (Lp; 8%–25%). Other particles that are much more abundant than in the KA samples are meta felsic (Lmv) and lithic limestone (Lcc) clasts (4%–17% and 9–16%, respectively). Volcanic mafic clasts (Lvm) are less abundant than in the KA samples and show a significant upsection decrease from 21% to 3%. Quartz (Figures 12e and 12i) and feldspar particles were also observed in GH sandstones (Figures 12d and 12h). Feldspar grains are less abundant than in the KA samples, with plagioclase particles ranging from 3 to 10%, while the alkali feldspars display also a very small amount (1%). Instead, Quartz grains are more abundant (9%–13%). A minor amount (≤3%) of other lithic fragments (Lvf, Lch, Lmf) and heavy minerals (such as epidote) were also observed.

Concerning the sedimentary paleocurrent directions, we do not have direct data for the TV and KA stratigraphic sections because we did not find suitable paleocurrent indicators in the field. Conversely, for the GH section we found a few wave ripples in the lacustrine deposits suggesting the occurrence of a paleo-shoreline parallel to the elongation of the basin (NW-SE). In addition, we observed imbricated clasts in alluvial-fan and fluvial deposits indicating a provenance from the northern basin margin.

4. Discussion

4.1. Magnetic Mineralogy

Demagnetization results suggest that samples from the TV and KA stratigraphic sections have a similar magnetic mineralogy. Specifically, the isolation of stable ChRM directions at temperatures between 300°C and 580°C and magnetic fields ranging from 15 to 120 mT indicates the occurrence of a magnetically soft, low-temperature mineral such as magnetite as main carrier of the ChRM. Few KA samples, however, contain higher temperature magnetic minerals that have an unblocking temperature between 600°C and 640°C, suggesting the occurrence of maghemite. Instead, GH samples contain both magnetically soft/low-temperature minerals such as magnetite and magnetically hard/high-temperature minerals such as hematite and maghemite. The presence of hematite is documented by unblocking temperatures of 650°C/680°C and in case of AF demagnetization by the occurrence of stable components that cannot be removed between 15 and 120 mT field peaks.

Sediment provenance data (Figure 12) indicate that sediments of the TV and KA stratigraphic sections (southern basin margin) were entirely sourced by volcanic rocks and volcanoclastic units, most likely belonging to the Karaj Formation (see also Section 4.3). Conversely, paleocurrent directions and sediment provenance data for the GH stratigraphic section (Figures 12 and 13; see also Section 4.3) suggest a composite sediment source area like the western Alborz Mountains, which consist of Eocene volcanic rocks, MesoPaleozoic clastic sediments and metamorphic units (Figures 1 and 2). Overall, this difference in the sediment source area is well reflected in the magnetic mineralogy (magnetite/maghemite for TV and KA vs. magnetite/maghemite/hematite for the GH section) and consequently in the bulk susceptibility values that are higher (at least one order of magnitude) for samples dominated by magnetite of the TV and KA sections.

4.2. Magnetostratigraphy

The VGP latitudes from the new paleomagnetic data set define normal and reverse polarity magnetozones (Figures 9e, 10e, and 11e) and hence allow constructing for each section a magnetic polarity stratigraphy to be correlated with the Neogene Geomagnetic Polarity Time Scale (GPTS) (Hilgen et al., 2012). In the following, we first correlate the KA section based on an independent radiometric age (sample TM-16-01), and then we correlate the underlying TV and the overlying GH stratigraphic sections.

4.2.1. KA Stratigraphic Section

In the KA stratigraphic Section 7 normal (N1–N7) and 8 reverse (R1–R8) polarity zones were defined (Figure 10). A Zircon U-Pb age of 10.7 ± 0.4 Ma (Table 1) from an ash layer in the upper part of the section at ∼500 m suggests that the long-lasting normal polarity zone N1 should be correlated with chron C5n1n. Consequently, the two short reverse polarity zones R1 and R2 and the longer normal polarity zone N2 should belong to the same C5 chron. According to these correlations, the polarity zones N3, N4, and N5 as well as the reverse polarity zones R3, R4, R5, and R6 should correspond to chron C5A (Figure 10). In the lower part of the section, the normal and reverse polarity zones N6 and R7 can be correlated with chron C5AA, while the long lasting normal polarity (N7) and the short reverse polarity zone at the base of the section can be correlated to chron C5AB (Figure 10). Note that the top of the sections falls within the same magnetozone, therefore, we cannot constrain the top age of the stratigraphic section. If we assume a constant sediment accumulation rate, the top age would be around 9 Ma (Figure 13), but this would require changes in the magnetic polarities that are not observed in our magnetic polarity stratigraphy. In such a case the top of the section should have been remagnetized during a period of normal polarity (most likely before folding because the data set passed the fold test) while the ash layer should be two million years younger than 10.7 ± 0.4 Ma (Figure 13). Alternatively, if there was an acceleration in the sediment accumulation rate, and we assume that the depositional age of the ash layer corresponds to our zircon U-Pb age of 10.7 ± 0.4 Ma, the top age of the section would fall into long lasting normal chron C5n1n and hence would be younger than ∼10 Ma (or ∼9.6 Ma, if we include in such a chron the two short-lasting reverse polarities that occurred between 10 and 9.6 Ma; Figure 13). This second option seems be less problematic, therefore, we tend to favor a top age of the KA section of <10 Ma. Instead, for the base of the section, we can assume an age of ∼13.6 Ma based on the correlation with chron C5AB (Figure 10). Therefore, the most likely depositional age for the KA stratigraphic section will be between ∼13.6 and probably <10 Ma (Figures 10 and 13).

4.2.2. TV Stratigraphic Section

Patterns of VGP latitudes in section TV define four normal and two reverse polarity zones denoted as N1–N4 and R1 and R2, respectively. Stratigraphically, the TV section lies underneath the KA stratigraphic section (Figure 2), thus we correlate the uppermost long normal polarity zone N1 and the reverse polarity zone R1 with chron C5AC. Consequently, the long normal polarity zone N2 in the middle part of the section is correlated with chron C5AD and the short normal polarity zone N3 with chron C5B. One reverse polarity zone in chron C5AD, one short normal as well as a reverse polarity zone in the upper part of chron C5B in the GPTS are missing in our records. Besides these three incompatibilities, which represent the time period between ~14.6 and 15.1 Ma, we successfully matched up each chron with the GPTS. We note that the missing chrons come from the lower part of the section where the sedimentation rate is lower (~0.025 mm/yr) (Figure 13) and the probability to miss a chron greater. The reverse polarity zone R2 in the lowermost part of the section should correspond to chron C5B, while the long normal polarity zone N4 at the base of the section should correlate with chron C5C. Accordingly, a depositional age of ~16.2 to 13.7 Ma is proposed for the TV stratigraphic section (Figures 9 and 13).

4.2.3. GH Stratigraphic Section

Patterns of VGP latitudes in section GH define 10 normal and 9 reverse polarity zones, denoted as N1–N10 and R1–R9, respectively. Stratigraphic sections KA and GH overlap, hence, in our tentative correlation we associate the long-lasting, distinctive normal polarity zone N1 of section KA with the normal zone N5 in the middle part of section GH. The uppermost normal polarity zones N1, N2, and N3 as well as the short reverse polarity zone R1 and long-lasting reverse polarity zones R2 and R3 at the top of the section can be correlated with chron C4. Consequently, the normal and reverse polarity zones N4 and R4 correlate with chron C4A. The long-lasting normal polarity zone N5 in the middle part of the section as well as the two short normal polarity zones N6 and N7 and two long reverse polarity zones R5 and R6 correspond to chron C5. Finally, the normal polarity zones N8, N9, and N10 and the reverse polarity zones R7, R8, and R9 in the lowermost part of the section should correlate with chron C5A. Based on this correlation the depositional age of section GH should range from ~13.2 to 7.6 Ma (Figures 11 and 13).

Combined our data document that sedimentation of the red beds in Tarom Basin initiated not later than ~16.2 Ma (see Section 4.4.2) and lasted at least until 7.6 Ma. Importantly, this implies that these red beds belong to the URF (see Section 4.4.2).

4.2.4. Sediment Accumulations Rates

The sediment accumulation rates for each stratigraphic section were calculated based on the magnetostratigraphic correlations and the stratigraphic (compacted) thickness measured in the field (Figure 13). The oldest record (from ~16.2 Ma) is from the TV section where rates are relatively low (0.025 mm/yr) until ~14.6 Ma when an increase up to ~0.1 mm/yr occurs. From ~13.6 Ma the record includes both the GH and KA sections with similar rates of ~0.21 mm/yr at least until ~12.1 Ma. By ~12.1 Ma, sediment accumulation rates for the GH section increase up to ~0.29 mm/yr and remain higher than those in the KA section (at least until the top of the KA section at ~10.3 Ma). At the top the section, sediment accumulation rates decrease down to 0.15 mm/yr. Note that we do not observe correlations between changes in depositional environments and acceleration-deceleration in the sediment accumulation rates as observed in foreland basins (e.g., Ballato & Strecker, 2014 and references therein). Overall, the sediment accumulation rates from the intermontane Tarom Basin are slightly lower than those recorded in the Miocene foreland basins of N Iran (0.3–2.2 and 0.3–0.5 mm/yr for the southern Alborz Mountains and the Great Pari Basin, respectively; Ballato et al., 2008, 2017) but they are still comparable with rates observed in tectonically active regions of the Alpine-Himalayan orogenic belt (e.g., Chang et al., 2012; Charreau et al., 2005; Huang et al., 2006; Zhu et al., 2008).

4.3. Sediments Provenance

The abundance of volcanic clasts in the KA samples indicates that sediments along the southern margin of the basin were sourced from the Eocene volcanic rocks of the Karaj Formation. Considering the proximity of the KA samples to the Tarom range, the presence of landslide deposits coming from the south embedded in the KA stratigraphic section (see Section 3.2.2; Paknia et al., 2019), and the occurrence of reworked Eocene zircons from the top of the Karaj Formation in red beds that represent the along strike continuation of the KA section (samples GH-17-02 and 04; Figures 1 and 7), we conclude that the KA stratigraphic section must have received sediments from the Tarom range. This applies also to the TV section, which is directly in contact with the Karaj Formation and is more proximal than the KA section. It should also be noted that while the thin sections from the KA samples do not present any clasts of intrusive rocks, the unconformable

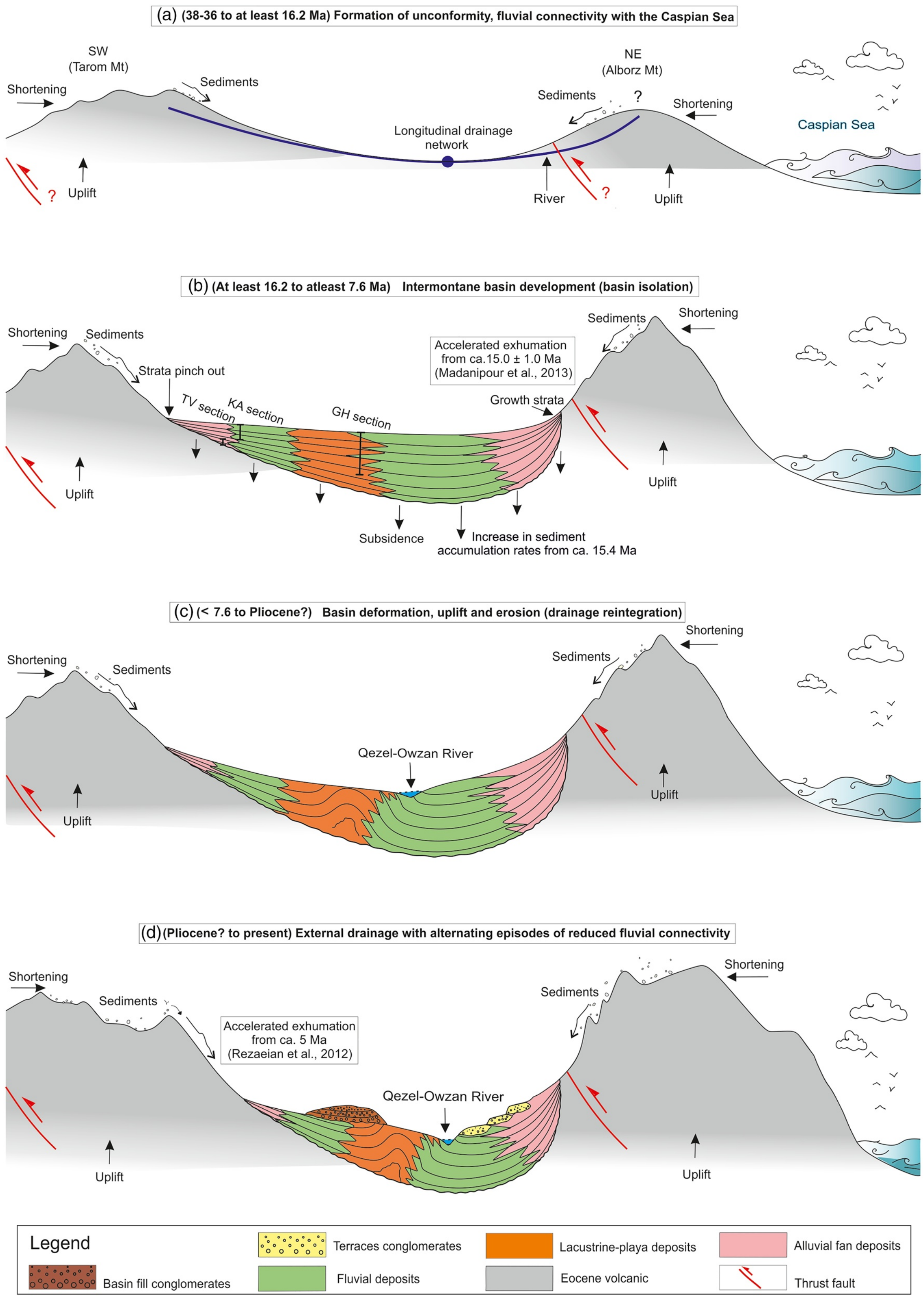
(a) (38-36 to at least 16.2 Ma) Formation of unconformity, fluvial connectivity with the Caspian Sea
SW
(Tarom Mt)
Shortening
Sediments
?
Uplift
Longitudinal drainage
network
River
NE
(Alborz Mt)
Sediments
?
Shortening
?
Uplift
Caspian Sea
(b) (At least 16.2 to atleast 7.6 Ma) Intermontane basin development (basin isolation)
Shortening
Sediments
Strata pinch out
TV section
KA section
GH section
Uplift
Accelerated exhumation
from ca.15.0 ± 1.0 Ma
(Madanipour et al., 2013)
Sediments
Shortening
Growth strata
Uplift
Subsidence
Increase in sediment
accumulation rates from ca. 15.4 Ma
(c) (< 7.6 to Pliocene?) Basin deformation, uplift and erosion (drainage reintegration)
Shortening
Sediments
Uplift
Qezel-Owzan River
Sediments
Shortening
Uplift
(d) (Pliocene? to present) External drainage with alternating episodes of reduced fluvial connectivity
Shortening
Sediments
Accelerated exhumation
from ca. 5 Ma
(Rezaeian et al., 2012)
Uplift
Qezel-Owzan River
Sediments
Shortening
Uplift
Legend
Basin fill conglomerates
Terraces conglomerates
Fluvial deposits
Lacustrine-playa deposits
Eocene volcanic
Alluvial fan deposits
Thrust fault

conglomerates of supposed Pliocene age contain abundant granitoid clasts, which are currently exposed along the southern slope of the range (Figures 1 and 2). This indicates a post 7.6 Ma exposure of the granitoids of the Tarom range and appears to be consistent with an increase in exhumation rates over the last 5 Ma revealed by low-temperature thermochronology data (Rezaeian et al., 2012).

Concerning the central sectors of the basin, the occurrence of metamorphic and sedimentary lithics, as well as the progressive upsection decrease in volcanic grains suggests that the GH samples were sourced from a composite sediment source area, and hence must have received a larger amount of sediments from the western Alborz Mountains (Figure 1). This agrees with paleocurrent directions from imbricated conglomerate clasts of the GH stratigraphic section (Figure 11).

4.4. Basin Evolution

4.4.1. ∼38-36 to Not Later Than 16.2 Ma: Topographic Growth of the Basin Margins, Formation of Angular Unconformities and Development of External Drainage Conditions

The geometrical relationships among the strata of the Karaj Formation exposed along the southern sectors of the Tarom Basin suggest that large scale tilting and minor folding must have occurred after the Eocene arc volcanism (post 38-36 Ma; Figures 3b, 3c, and 7). Contractional deformation occurred also along the northern basin margin (Alborz Mountains) as indicated by the presence of a pronounced angular unconformity between the base of the red beds and the deposits of the Karaj Formation (Figures 3d and 4). Low-temperature thermochronology data suggest that the post 38-36 Ma deformation should have been associated with erosional cooling along both margins (see bedrock late Eocene to Oligocene apatite fission tracks cooling ages reported in Rezaeian et al., 2012 and the peak age of detrital apatite fission tracks of 27 ± 1.9 Ma, reported in Madanipour et al. [2013]). In addition, contraction must have produced topographic growth of the Tarom range leading to the isolation of the Tarom Basin from Central Iran. This hampered the regional late Oligocene-early Miocene marine transgression and the deposition of the shallow water marine limestones of the Qom Formation (Figure 1; Reuter et al., 2009). Topographic growth should have also occurred along the western Alborz Mountains, although it should be noted that the northern sectors of the range must have represented a topographic barrier between Central Iran and the Caspian Sea since the early Eocene as suggested by the spatial distribution of Karaj Formation (Figure 1; Guest, Axen et al., 2006). The post 38-36 Ma contractional deformation and associated erosional cooling may represent the earliest stages of late Eocene-early Oligocene collisional deformation recorded across the entire Arabia-Eurasia collision zone from the Zagros to the Caucasus, Talesh, Alborz and Kopeh Dagh mountains (Ballato et al, 2011, 2015; Morley et al., 2009; Mouthereau et al., 2012; Rezaeian et al., 2012; Roberts et al., 2014; Tadayon et al., 2018; S. J. Vincent et al., 2007). Sedimentation resumed not later than 16.2 Ma (see next section), therefore between 38 and 36 Ma and not later than 16.2 Ma, the Tarom Basin must have experienced erosion and nondeposition in association with external drainage conditions (Figure 14a). This implies that the sediments eroded along the margins of the Tarom Basin must have been delivered directly to the Caspian Sea, rather than being stored in the basin itself.

4.4.2. Not Later Than 16.2 to <7.6 Ma: Intermontane Basin Development and Internal Drainage Conditions

Sedimentation of the continental red beds of the Tarom Basin started not later than 16.2 Ma and lasted at least until 7.6 Ma. The 16.2 Ma age represents a minimum depositional age because sedimentation in the central sectors of the basin may have started a bit earlier. The lack of exposures of the base of the red beds in the central sectors of the basin hampers a more precise age determination. Importantly, our new ages documents that the red beds of the Tarom Basin are strati-

Figure 14. Schematic diagram showing the late Cenozoic evolution of the Tarom Basin (a) ∼38-36-16.2 Ma, uplift and tilting, formation of angular unconformities, and development of an external drainage system flowing into the Caspian Sea. (b) ∼16.2-7.6 Ma, basin isolation and internal drainage conditions, development of an intermontane basin, uplift of the basin-bounding mountain ranges (Tarom and Alborz ranges). The red bars show the location of three measured stratigraphic sections (c) ∼7.6 Ma-Pliocene? drainage reintegration with renewed fluvial connectivity with the Caspian Sea, intrabasinal deformation, basin uplift and erosion. (d) Pliocene? to present, cycles of incision and aggradation, folding of basin fill conglomerates.

graphically equivalent to the URF, a well-known Middle to Late Miocene formation that is, widely exposed in the southern margin of the Eurasian upper plate (Figure 1; e.g., Ballato et al., 2008, 2017 and references therein).

The occurrence of lacustrine and playa lake deposits in the basin depocenter implies the development of internally drained conditions associated with the topographic growth of the western Alborz Mountains, which must have disconnected the former drainage system from the Caspian Sea. Such a topographic growth was triggered by widespread regional deformation related to a more advanced stage of the Arabia-Eurasia collision (e.g., Ballato et al., 2011; Mouthereau et al., 2012) in agreement with available low-temperature thermochronology data (Ballato et al., 2013, 2015; Guest, Stockli et al., 2006; Madanipour et al., 2013, 2017; Rezaeian et al., 2012) and the tectono-stratigraphic evolution of sedimentary basins (Ballato et al., 2008, 2017; Guest et al., 2007) in northern Iran.

Importantly, the development of the Tarom Basin was associated with a sharp increase in sediment accumulation rates from 0.025 to 0.1 mm/yr along the TV section at ~14.6 Ma (Figure 13). This acceleration correlates very well with detrital apatite fission tracks ages from rivers draining the western Alborz Mountains. Specifically, Madanipour et al (2013) found that in the Southern Talesh, about one-third of their detrital ages belongs to a population that has a peak age of 15.0 ± 1.0 Ma (later revised to 13.0 ± 1.2 Ma; Madanipour et al., 2017), indicating a Middle Miocene acceleration in erosional exhumation induced by collisional deformation. This is also consistent with the occurrence of growth strata along the northern margin of the Tarom Basin, that testify syndepositional contractional deformation (Figures 4 and 14b). Combined, these observations suggest that the Tarom Basin must have formed as flexural response to tectonic loading from the uplifting bounding ranges (Figure 14b).

Tectonic load, however, must have been greater along the northern side of the basin. This because the western Alborz Mountains are characterized by reset apatite fission track data indicating more than 4 km of exhumation (Madanipour et al., 2013, 2017), while in the Tarom range, available apatite fission track data are mostly unrest to partially reset indicating less than 3–4 km of erosional exhumation (Rezaeian et al., 2012). The occurrence of limited erosional exhumation in the Tarom range is further supported by subdued topography onlapped by basin-fill units of the plateau interior along the northern sectors of the range (Heidarzadeh et al., 2017).

Overall, these conclusions are consistent with our sediment provenance data. Sandstone samples from the GH section contains a higher proportion of metamorphic lithics and quartz grains (quartzo-lithic arenite; Figure 12b) suggesting that the central part of the basin received a greater amount of sediments from the growing western Alborz Mountains. The upsection increase in metamorphic grains and the relative decrease in volcanic lithics indicates erosional unroofing with the progressive exposure of the metamorphic basement (Figure 12a). Furthermore, our sedimentologic and paleocurrent study show the occurrence of short- (probably a few tens or hundreds of thousand years) to long-lasting periods (up to ~1 Ma) of southward progradation of coarse-grained facies over lacustrine/playa lake sediments (Figure 13) that could have recorded enhanced phases of sediment supply (Ballato & Strecker, 2014). Conversely, the southern side of the basin received sediments from the growing Tarom range as documented by sandstone samples from the KA stratigraphic section that exhibit a rather constant modal composition dominated by volcanic lithics and feldspars (feldspatho-lithic arenite; QFL plot; Figure 12b). This composition is consistent with an undissected volcanic arc (QtFL-c ternary diagram; Figure 12a) represented by the deposits of the Karaj Formation.

4.4.3. <7.6 Ma to Pliocene? Drainage Reintegration, Basin Uplift, Deformation, and Erosion

Sometime after ~7.6 Ma, sedimentation in the Tarom Basin ended, and hence the sediments eroded from the growing mountains must have been transported somewhere else. This suggests that the basin must have been reintegrated into an external drainage system and a new fluvial connection with the Caspian Sea must have developed. One possible cause could be fluvial headward erosion triggered by the km-scale, base level drop of the Caspian Sea between ~5.5 and 3 Ma (Forte & Cowgill, 2013). Alternatively, basin capture may have occurred through overspill from the Tarom Basin into the Caspian Sea. In any case, after 4 Ma, the Tarom Basin must have been integrated into the drainage system of the Qezwl-Owzan as documented by

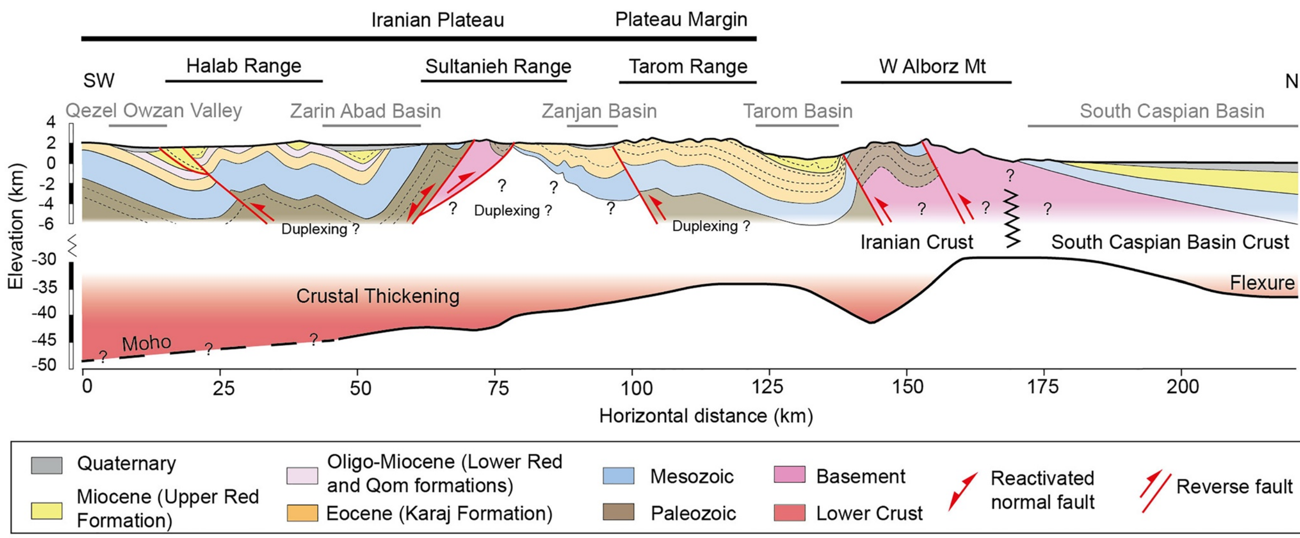

Figure 15. Geologic cross section (see Figure 1 for location) across the IP and its northern margin based on Stocklin and Eftekharnezhad (1969) and R. G. Davies (1977) and our field observations The Moho depth (solid line) is from Motaghi et al., (2018). The dashed line is extrapolated from the trend in crustal thickness across the IP shown in Rahmani et al. (2019).

overflow processes from the adjacent and more elevated Mianeh Basin of the IP that led to the development of ∼1-km-deep Amardos gorge (Figure 1; Heidarzadeh et al., 2017). This implies that at least by 4 Ma, the Tarom Basin must have been integrated into a much large drainage basin that included sectors of the IP interior. It should be noted that the establishment of an external drainage system appears to coincide with intrabasinal deformation, basin uplift and erosion, as recorded by several post 7.6 Ma anticline-syncline pairs Tarom Basin (Figures 2, 4g, and 5). This is well visible in the central sectors of the study area (GH section) where the occurrence of subvertical to overturned red beds suggests the development of a north verging anticline most likely associated with a detachment horizon within gypsum layers at the base of the red beds (Figure 14). Finally, it should be noted that sometime after ∼7 Ma, oroclinal bending occurred all around Northern Iran, from the central Alborz Mountain to the Kopeh Dagh (Cifelli et al., 2015; Mattei et al., 2017, 2019). Paleomagnetic data from the Tarom Basin (Mattei et al., 2017), together with our equal area stratigraphic plots for the three stratigraphic sections (Figure 8b) show very limited clockwise or no rotations in this sector of the orogen. Thus we conclude that oroclinal bending did not have a significant impact on the post 7 Ma, basin fill history.

4.4.4. Pliocene? To Present: Alternating Episodes of Basin Aggradation, Incisions, and Excavation

Following intrabasinal deformation, the Tarom Basin experienced at least one major episode of (supposed) Pliocene conglomerate deposition (Stocklin, 1969, Figure 3a) as well as three main phases of basin aggradation and incision, as documented by distinct levels of Quaternary terrace conglomerates (Figures 2, 3a, 3g, and 14d). These unconformable deposits suggest the occurrence of alternating phases of limited (or absent) and efficient fluvial connectivity with the Caspian Sea. A similar configuration has been described in the intermontane basins of arid to semiarid climatic regions like those forming the Eastern Cordillera and the broken foreland of NW Argentina. There, the landscape response to Quaternary climate changes is thought to be the main driver of short-term cycles (10^5 years) of basin filling and excavation, while tectonics plays a major role in controlling the long-term filling history (10^6 years; Ballato et al., 2019; Pingel et al., 2019b; T. Schildgen et al., 2016; Strecker et al., 2009; Streit et al., 2015; Tofelde et al., 2017). Here, the lack of chronological constraints does not allow unraveling the role of different forcing mechanisms. In any case, it should be noted that, the supposed Pliocene conglomerates are slightly folded into a broad syncline suggesting a possible interplay between intrabasinal deformation and sedimentary loading/unloading cycles, which can hinder/promote intrabasinal deformation (Ballato et al., 2019). For example, these conglomerates are in unconformity onto folded Miocene red beds, therefore, their deformation must have occurred after their deposition either during or after their removal through fluvial erosion (i.e., during sedimentary unloading). The occurrence of supposed Pliocene conglomerates in proximity of the southern basin margin is consistent with an acceleration in exhumation rates along the Tarom range over the last 5 Ma (Rezaeian et al., 2012).

Finally, it should be noted that a similar long-term, tectono-stratigraphic history has been proposed for the intermontane Taleghan-Alamut Basin of the central-western Alborz Mountains (Figure 1; Guest et al., 2007). There, the deposition of middle-late Miocene red beds was followed by late Miocene-Pliocene intrabasinal deformation, Pliocene aggradation with conglomerate deposition and Quaternary fluvial incision. This common evolution suggests that the orogen may have responded along strike in a similar way to (either tectonic or climatic) forcing mechanisms (Ballato et al., 2015).

4.5. Implications for the Lateral Expansion of the IP

Our multidisciplinary approach allows elaborating a four-stage evolutionary model (Figure 14), that includes episodes of external drainage (stage 1, 38-36 Ma to not later than 16.2 Ma, and stage 3, <7.6 to Pliocene?), internal drainage (stage 2, not later than 7.6 Ma to Pliocene?) and limited connectivity with the foreland (stage 4, Pliocene? to present). Phases of internal drainage during continuous shortening are thought to promote the progressive incorporation of the foreland into the plateau as suggested for Tibet (e.g., Métivier et al., 1998). A similar pattern, although less systematic, has been also suggested for the Puna-Altiplano Plateau (Strecker et al., 2009 and references therein). Overall, this mechanism can be responsible for a lateral expansion (orogen perpendicular) of an orogenic plateau (e.g., Castellanos et al., 2007; Sobel et al., 2003). These observations suggest that Tarom Basin may have been part of the IP sometimes during the last 16 Ma and hence the plateau may have reduced its lateral size after fluvial capture.

Currently, there is a substantial difference between the topographic relief within the interior of the IP (<1 km between the Tarom range and the adjacent Zanjan Basin) and across its northern margin (>2 km between the Tarom range and Tarom Basin; Figures 1 and 15). This marks a clear morphological boundary between the plateau and the adjacent areas (Figure 1). Although we do not have yet data about the paleo-altimetric evolution of NW Iran, our field observations suggest that during phases of internal drainage or limited connectivity with the Caspian Sea, the Mio-Pliocene basin-filling processes did not produce an increase in the mean basin elevation up to the altimetry of the sedimentary basins of the plateau interior (Figures 1 and 15). This implies that a paleo-topographic relief between the Tarom Basin and the plateau margin must have existed for a long time. Consequently, the Tarom Basin was never morphologically incorporated into the plateau realm and the lateral (orogen perpendicular) size of the plateau has not decreased through time.

4.6. Implications for Vertical Growth of the IP Margin

Concerning the vertical evolution of the plateau margin, our provenance study and available low-temperature thermochronology data (see Section 4.2.2.) suggest that most of the Miocene convergence in NW Iran was absorbed via crustal shortening and thickening in the western Alborz Mountains rather than along the northern plateau margin (Tarom range). These observations agree with a recent seismological study documenting a Moho depth of at least 45 km in the plateau interior that tapers northward to ~35 km underneath the northern plateau margin and increases up to more than 40 km beneath the western Alborz (Figure 15; Motaghi et al., 2018). These data show that although the Tarom range is at least 1 km higher than the plateau interior it has a lower crustal thickness (~35 vs. 40–45 km; Figure 15). In addition, it shows that although the western Alborz Mountains have crust that is, up to a 5 km thicker than the crust of the Tarom range, the topographic elevation is quite similar (while it should be 1 km higher in the Alborz assuming Airy isostasy and typical crustal and mantle densities of 2.7 and 3.3 gr/cm^3, respectively). This suggests that isostasy is not respected and hence crustal thickening cannot be responsible for the topographic growth of the plateau margin. Consequently, the vertical growth of the Tarom range must have been triggered by deep-seated, mantle driven processes (e.g., Hatzfeld & Molnar, 2010) rather than crustal/lithospheric shortening and thickening (e.g., Sobel et al., 2003). One possible cause could be the large scale removal of dense lithospheric mantle (delamination) followed by upwelling of less dense and hot asthenospheric mantle (François et al., 2014b; Hatzfeld & Molnar, 2010), sometime between 12 and 10 Ma when deformation processes across the plateau interior appear to have accelerated (François et al., 2014a). An alternative model suggests that surface uplift may have been triggered by the establishment of a large-scale convective cell from the Afar plume to the collision zone following the break-off of the Neo-Tethys slab in front of the Arabian indenter at ~10 Ma (Faccenna et al., 2013). Slab-break off alone, however, could have also produced asthenospheric upwelling and surface uplift without invoking convective cells as suggested for Eastern Anatolia (T. F. Schildgen et al., 2014). All these models are in agreement with the occurrence of a thin lithospheric mantle and hot shallow asthenosphere across most of the upper plate from the suture zone to the shoreline of the Caspian Sea (Rahmani et al., 2019, and references therein). The presence of shallow asthenosphere is also supposed to be responsible for the late Miocene-Quaternary magmatism of NW Iran that led to the development of the Saray and Sahand volcanos in the internal domains of the plateau (~280 and 200 km to the NW of the Tarom Basin, respectively) and the Sabaland volcano along the plateau margin (~150 km to the NNW of the Tarom Basin). These volcanos have been active at ~11 Ma, and from ~8 to 0.17 Ma and ~4.5 to 0.15 Ma, respectively, and are characterized by a variable potassic to high-K calcalkaline and adakitic geochemical signatures and are considered the first evidence of post collisional magmatism (see a recent review of Rabiie et al., 2020).

In conclusion, our study allow us to: (1) corroborate the idea that topographic ponding alone in intermontane basins cannot produce high plateau elevations without a deep-seated, either lithospheric or asthenospheric support (Strecker et al., 2009); (2) infer that the topographic growth of the northern margin of the IP (Tarom range) is not caused by crustal thickening but rather deep-seated, possibly asthenospheric, processes (Faccenna et al., 2013; François et al., 2014b; Hatzfeld & Molnar, 2010; T. F. Schildgen et al., 2014).

5. Conclusions

Based on the new age determinations, the reconstruction of the depositional systems, and the provenance data, we propose a four-stage evolutionary model for the Tarom Basin for the last ~38-36 Ma (Figures 14a–14d) and we discuss the main implications of our findings for the lateral (orogen perpendicular) evolution of the IP, including the mechanisms that led to the growth of its northern margin (Figure 15). Our work represents the first detailed study in the Tarom Basin, an intermontane basin at the transition between the IP and the western Alborz Mountains. Combined, our data show that the regional, Eocene arc volcanism in NW Iran ended at ~38-36 Ma and was followed by low-magnitude compressional deformation in agreement with other studies conducted in the central Alborz Mountains (Ballato et al., 2011; Madanipour et al., 2017), and in the Urumieh Doktar Magmatic Zone (Morley et al., 2009; Verdel et al., 2011) This was followed by a prolonged phase of erosion with development of angular unconformities.

In the middle Miocene (not later than ~16.2 Ma) the topographic growth on the northern side of the basin (western Alborz Mountains) disconnected the Tarom Basin from the Caspian Sea, leading to the formation of an internally drained intermontane basin and to the deposition of clastic red beds. Our new ages document that these synorogenic deposits are stratigraphically equivalent to the Miocene URF. The accommodation space available for sedimentation was most likely controlled by lithospheric flexure in response to tectonic loading of the western Alborz Mountains. Internal drainage conditions and red beds sedimentation lasted at least until ~7.6 Ma, when basin incision and excavation occurred in association with intrabasinal deformation. Subsequently the occurrence of supposed Pliocene conglomerates and at least three Quaternary terrace conglomerates indicate multiple phases of aggradation and incision. This cyclic behavior occurred during alternating episodes of reduced and renewed fluvial connectivity with the Caspian Sea. The lack of a detailed chronology, however, does not allow understanding the forcing mechanisms for these cycles. The elevation of the Tarom Basin during endorheic conditions did not reach those of the intermontane basins of the plateau interiors, therefore, the basin was not morphologically integrated into the plateau, implying that basin filling and ponding processes cannot be responsible for surface uplift with a deep-seated (lithospheric or asthenospheric) support. Furthermore, the northern margin of the plateau (Tarom Range) experienced limited Miocene erosional exhumation and crustal shortening and thickening, as documented by our provenance study, low-temperature thermochronology and seismic data. Specifically, a recent image of the Moho depth indicates that the vertical growth of the plateau margin must have been triggered by deep-seated processes (delamination of thickened lithospheric mantle?) rather than crustal shortening and thickening.

Data Availability Statement

Software and analyzed data of paleomagnetic samples used to produce the results in this work are available at https://data.mendeley.com/datasets/n5z4h9dy6x/2/ and DOI:10.17632/n5z4h9dy6x.2. We thank the Editor Taylor Schildgen and the Associate Editor Derya Guerer for their assistance and suggestions and we are grateful to Renas Koshnaw and three anonymous reviewers for the constructive comments. The authors would also like to thank Masoud Biralvand and Mahmood Fallah for helping with the logistic during the field work.

Acknowledgments
This study is part of the PhD thesis of MP at the University of Roma Tre (PhD program Cycle XXXII) and was supported by the PhD School of Roma Tre, the MIUR (Ministry of Education University and Research: Grant Rita Levi Montalcini and Prin_2017 20177BX42Z to PB, and Prin_2015 20158A9CBM_002 to MM), the DFG (German Science Foundation: grants DFG BA 4420/2-1 and BA 4420/2-2 to PB) and the DAAD (German Academy Research Service, grant to GH). The authors declare no financial or other conflicts of interest.

References

Abimbola, D. A. (2016). A Re-evaluation of the Depositional Environments and Sedimentary Facies of Middle Miocene Paralic Deposits (Agbada Formation), Ewan and Oloye Fields, Northwestern Niger Delta. *Journal of Marine Science: Research & Development*, *6*(193), 2. https://doi.org/10.4172/2155-9910.1000193

Agard, P., Omrani, J., Jolivvet, L., Whitechurch, H., Vrielynck, B., Spakman, W., et al. (2011). Zagros orogeny: A subduction-dominated process. *Geological Magazine*, *148*(5–6), 689–691. https://doi.org/10.1017/S001675681100046X

Alonso, B., E Field, M., V Gardner, J., & Maldoando, A. (1990). Sedimentary evolution of the Pliocene and Pleistocene Ebro margin, northeastern Spain. *Marine Geology*, *95*(3–4), 313–331.

Amini, B. (1969). *Geological map of Tarom*. Tehran: Geological Survey of Iran.

Ballato, P., Brune, S., & Strecker, M. R. (2019). Sedimentary loading–unloading cycles and faulting in intermontane basins: Insights from numerical modelling and field observations in the NW Argentine Andes. *Earth and Planetary Science Letters*, *506*, 388–396. https://doi.org/10.1016/j.epsl.2018.10.043

Ballato, P., Cifelli, F., Heidarzadeh, G. H., Ghassemi, M. R., Wicert, A. D., Hassanzadeh, J., et al. (2017). Tectono-sedimentary evolution of the northern Iranian Plateau: Insights from middle-late Miocene foreland-basin deposits. *Basin Research*, *29*(4), 417–446. https://doi.org/10.1111/bre.12180

Ballato, P., Landgraf, A., Fox, M., Stockli, D., Schildgen, T. F., Ghassemi, M. R., et al. (2015). The growth of a mountain belt forced by base-level fall: Tectonics and surface processes during the evolution of the Alborz Mountains, N Iran. *Earth and Planetary Science Letters*, *425*, 204–218. https://doi.org/10.1016/j.epsl.2015.05.051

Ballato, P., Nowaczy, N. R., Landgraf, A., Strecker, M. R., Friedrich, A., & Tabaei, S. H. (2008). Tectonic control on sedimentary facies pattern and sediment accumulation rates in the Miocene foreland basin of the southern Alborz mountains, northern Iran. *Tectonics*, *27*(6). TC6001. https://doi.org/10.1029/2008TC002278

Ballato, P., Stockli, D. F., Ghassemi, M. R., Landgraf, A., Strecker, M. R., Hassanzadeh, J., et al. (2013). Accommodation of transpressional strain in the Arabia-Eurasia collision zone: New constraints from (UTh)/He thermochronology in the Alborz mountains, north Iran. *Tectonics*, *32*(1), 1–18. https://doi.org/10.1029/2012TC003159

Ballato, P., & Strecker, M. R. (2014). Assessing tectonic and climatic causal mechanisms in foreland-basin stratal architecture: Insights from the Alborz Mountains, northern Iran. *Earth Surface Processes and Landforms*, *39*(1), 110–125. https://doi.org/10.1002/esp.3480

Ballato, P., Uba, C. E., Landgraf, A., Strecker, M. R., Sudo, M., Stockl, D. F., et al. (2011). Arabia-Eurasia continental collision: Insights from late Tertiary foreland-basin evolution in the Alborz Mountains, northern Iran. *Geological Society of America Bulletin*, *123*(1–2), 106–131. https://doi.org/10.1130/B30091.1

Barber, D. E., Stockli, D. F., Horton, B. K., & Koshnaw, R. I. (2018). Cenozoic exhumation and foreland basin evolution of the Zagros orogen during the Arabia-Eurasia collision, western Iran. *Tectonics*, *37*(12), 4396–4420 https://doi.org/10.1029/2018TC005328

Berberian, M., & Walker, R. (2010). The Rudbār Mw 7.3 earthquake of 1990 June 20; seismotectonics, coseismic and geomorphic displacements, and historic earthquakes of the western 'High-Alborz', Iran. *Geophysical Journal International*, *182*(3), 1577–1602. https://doi.org/10.1111/j.1365-246X.2010.04705.x

Blair, T. C. (1999). Sedimentology of the debris-flow–dominated Warm Spring Canyon alluvial fan, Death Valley, California. *Sedimentology*, *46*(5), 941–965. https://doi.org/10.1046/j.1365-3091.1999.00260.x

Boothroyd, J. C., & Ashley, G. M. (1975). *Processes, bar morphology, and sedimentary structures on braided outwash fans, northeastern Gulf of Alaska*. The Society of Economic Paleontologists and Mineralogist (SEPM); Glaciofluvial and Glaciolacustrine Sedimentation (SP23).

Borradaile, G. J. (1988). Magnetic susceptibility, petrofabrics and strain. *Tectonophysics*, *156*(1–2), 1–20. https://doi.org/10.1016/0040-1951(88)90279-X

Borradaile, G. J. (2001). Magnetic fabrics and petrofabrics: Their orientation distribution and anisotropies. *Journal of Structural Geology*, *23*(10), 1581–1596. https://doi.org/10.1016/S0191-8141(01)00019-0

Borradaile, G. J., & Henry, B. (1997). Tectonic applications of magnetic susceptibility and its anisotropy. *Earth-Science Reviews*, *42*(1–2), 49–93. https://doi.org/10.1016/S0012-8252(96)00044-X

Brunet, M., Korotaev, M. V., Ershov, A. V., & Nikishin, A. M. (2003). The South Caspian Basin: A review of its evolution from subsidence modelling. *Sedimentary Geology*, *156*(1–4), 119–148. https://doi.org/10.1016/S0037-0738(02)00285-3

Bush, M.A., Saylor, J.E., Horton, B.K., & Nie, J. (2016). Growth of the Qaidam Basin during Cenozoic exhumation in the northern Tibetan Plateau: Inferences from depositional patterns and multiproxy detrital provenance signatures. *Lithosphere*, *8*(1), 58–82. https://doi.org/10.1130/L449.1

Carroll, A. R., Graham, S. A., & Smith, M. E. (2010). Walled sedimentary basins of China. *Basin Research*, *22*(1), 17–32. https://doi.org/10.1111/j.1365-2117.2009.00458.x

Castellanos, D. G. (2007). The role of climate during high plateau formation. Insights from numerical experiments. *Earth and Planetary Science Letters*, *257*(3–4), 372–390. https://doi.org/10.1016/j.epsl.2007.02.039

Castro, A., Aghazadeh, M., Badrzadeh, Z., & Chichorro, M. (2013). Late Eocene–Oligocene post-collisional monzonitic intrusions from the Alborz magmatic belt, NW Iran. An example of monzonite magma generation from a metasomatized mantle source. *Lithos*, *180–181*, 109–127. https://doi.org/10.1016/j.lithos.2013.08.003

Chadima, M., & Hrouda, F. (2006). Remasoft 3.0 a user-friendly paleomagnetic data browser and analyzer. *Travaux Géophysiques*. *27*(XXVII:20–21).

Chakraborty, T., & Sarkar, S. (2005). Evidence of lacustrine sedimentation in the Upper Permian Bijori Formation, Satpura Gondwana basin: Palaeogeographic and tectonic implications. *Journal of Earth System Science*, *114*(3), 303–323. https://doi.org/10.1007/BF02702952

Chang, H., An, Z., Liu, W., Qiang, X., Song, Y., & Ao, H. (2012). Magnetostratigraphic and paleoenvironmental records for a Late Cenozoic sedimentary sequence drilled from Lop Nor in the eastern Tarim Basin. *Global and Planetary Change*, *80–81*, 113–122. https://doi.org/10.1016/j.gloplacha.2011.09.008

Charreauh, J., Chen, Y., Gilder, S., Dominguez, S., Avouac, J.-P., Sen, S., et al. (2005). Magnetostratigraphy and rock magnetism of the Neogene Kuitun He section (northwest China): Implications for Late Cenozoic uplift of the Tianshan mountains. *Earth and Planetary Science Letters*, *230*(1–2), 177–192. https://doi.org/10.1016/j.epsl.2004.11.002

Cifelli, F., Ballato, P., Alimohammadian, H., Sabouri, J., & Mattei, M. (2015). Tectonic magnetic lineation and oroclinal bending of the Alborz range: Implications on the Iran-Southern Caspian geodynamics. *Tectonics*, *34*(1), 116–132. https://doi.org/10.1002/2014TC003626

Davies, D., Suppe, J., & Dahlen, F. A. (1983). Mechanics of fold-and-thrust belts and accretionary wedges. *Journal of Geophysical Research*, *88*(B2), 1153–1172.

Davies, R. G. (1977). *Geological map of Bandar e Pahlavi quadrangle*. Tehran: Geological Survey of Iran.

Davoudzadeh, M., Lammerer, B., & Weber-Diefenbach, K. (1997). Paleogeography, stratigraphy, and tectonics of the tertiary of Iran. *Neues Jahrbuch für Geologie und Paläontologie – Abhandlungen*, *205*(1), 33–67.

Dewey, J. F. (1988). Extensional collapse of orogens. *Tectonics*, *7*(6), 1123–1139.

Dewey, J. F., & Burke, K. (1974). Hot spots and continental break-up: Implications for collisional orogeny. *Geology*, *2*(2), 57–60.

Dickinson, W. R. (1985). Interpreting provenance relations from detrital modes of sandstones. In G. G. Zuffa (Ed.), Provenance of arenites. Vol. 148 (pp. 333–361). Dordrecht: Reidel, NATO ASI Series.

Djamour, Y., Vernant, P. H., Bayer, R., Nankali, H. R., Ritz, J. F., Hinderer, J., et al. (2010). GPS and gravity constraints on continental deformation in the Alborz Mountain range, Iran. *Geophysical Journal International*, *183*(3), 1287–1301. https://doi.org/10.1111/j.1365-246X.2010.04811.x

Dupont-Nivet, G., & Krijgsman, W. (2012). Magnetostratigraphic methods and applications. In C. Busby & A. Azor (Eds.), *Recent advances in tectonics of sedimentary basins* (pp. 80–94). Wiley-Blackwell.

Ejiuba, C., Heubeck, C., & Hulka, C. (2005). Facies analysis and basin architecture of the Neogene Subandean synorogenic wedge, southern Bolivia. *Sedimentary Geology*, *180*(3–4), 91–123. https://doi.org/10.1016/j.sedgeo.2005.06.013

Engdahl, E., Jackson, J., Myers, S., Bergman, E., & Priestley, K. (2006). Relocation and assessment of seismicity in the Iran region. *Geophysical Journal International*, *167*(2), 761–788. https://doi.org/10.1111/j.1365-246X.2006.03127.x

England, P. H., & McKenzie, D. (1982). A thin viscous sheet model for continental deformation. *Geophysical Journal International*, *70*(2), 295–321.

Faccenna, C., Becker, T. W., Jolivet, L., & Keskin, M. (2013). Mantle convection in the Middle East: Reconciling Afar upwelling, Arabia indentation and Aegean trench rollback. *Earth and Planetary Science Letters*, *375*, 254–269. https://doi.org/10.1016/j.epsl.2013.05.043

Fisher, R. A. (1953). Dispersion on a sphere. *Proceedings of the Royal Society of London, Series A*, *217*(1130), 295–305.

Forte, A. M., & Cowgill, E. (2013). Late Cenozoic base-level variations of the Caspian Sea: A review of its history and proposed driving mechanisms. *Palaeogeography, Palaeoclimatology, Palaeoecology*, *386*, 392–407. https://doi.org/10.1016/j.palaeo.2013.05.035

François, T., Agard, P., Bernet, M., Meyer, B., Chung, S. L., Zarrinkoub, M. H., et al. (2014a). Cenozoic exhumation of the internal Zagros: First constraints from low-temperature thermochronology and implications for the build-up of the Iranian plateau. *Lithos*, *206–207*, 100–112. https://doi.org/10.1016/j.lithos.2014.07.021

François, T., Burov, E., Agard, P., & Meyer, B. (2014b). Buildup of a dynamically supported orogenic plateau: Numerical modeling of the Zagros/Central Iran case study. *Geochemistry, Geophysics, Geosystems*, *15*(6), 2632–2654. https://doi.org/10.1002/2013GC005223

Gansser, A. (1958). *The general geology of Iran*. NIOC, Geological Report No. 194.

Garzanti, E. D. (2019). Petrographic classification of sand and sandstone. *Earth-Science Reviews*, *192*, 545–563. https://doi.org/10.1016/j.earscirev.2018.12.014

Ghibaudo, G. U. (1992). Subaqueous sediment gravity flow deposits: Practical criteria for their field description and classification. *Sedimentology*, *39*(3), 423–454.

Ghinass, M., D'oriano, F., Benvenuti, M., Fedi, M., & Awramik, S. (2015). Lacustrine facies in response to millennial-century-scale climate changes (Lake Hayk, Northern Ethiopia). *Journal of Sedimentary Research*, *85*(4), 381–398. http://dx.doi.org/10.2110/jsr.2015.28

Gradstein, F. M., Ogg, J. G., Schmitz, M., & Ogg, G. (2012). *The geologic time scale 2012*. Cambridge: Elsevier, Cambridge University Press.

Guest, B., Axen, G. J., Lam, P. S., & Hassanzadeh, J. (2006). Late Cenozoic shortening in the west central Alborz Mountains, northern Iran, by combined conjugate strike-slip and thin-skinned deformation. *Geosphere*, *2*(1), 35–52. https://doi.org/10.1130/GES00019.1

Guest, B., Horton, B. K., Axen, G. J., Hassanzadeh, J., & Mcintosh, W. C. (2007). Middle to late Cenozoic basin evolution in the western Alborz Mountains: Implications for the onset of collisional deformation in northern Iran. *Tectonics*, *26*(6). TC6011. https://doi.org/10.1029/2006TC002091

Guest, B., Stockli, D. F., Grove, M., Axen, G. J., Lam, P. S., & Hassanzadeh, J. (2006). Thermal histories from the central Alborz Mountains, northern Iran: Implications for the spatial and temporal distribution of deformation in northern Iran. *Geological Society of America Bulletin*, *118*(11–12), 1507–1521. https://doi.org/10.1130/B25819.1

Hassanzadeh, J., Stockli, D. F., Horton, B. K., Axen, G. J., Stockl, L. D., & Grove, M. (2008). U-Pb zircon geochronology of late Neoproterozoic-Early Cambrian granitoids in Iran: Implications for paleogeography, magmatism, and exhumation history of Iranian basement. *Tectonophysics*, *451*(1–4), 71–96. https://doi.org/10.1016/j.tecto.2007.11.062

Hatzfeld, D., & Molnar, P. (2010). Comparisons of the kinematics and deep structures of the Zagros and Himalaya and of the Iranian and Tibetan plateaus and geodynamic implications. *Reviews of Geophysics*, *48*(2), RG2005. https://doi.org/10.1029/2009RG000304

Heidarzadeh, G. H., Ballato, P., Hassanzadeh, J., Ghassemi, M. R., & Strecker, M. R. (2017). Lake overspill and onset of fluvial incision in the Iranian Plateau: Insights from the Mianeh Basin. *Planetary Science Letters*, *469*, 135–147. https://doi.org/10.1016/j.epsl.2017.04.019

Hein, F. J. (1982). Depositional mechanisms of deep-sea coarse clastic sediments, Cap Enrage Formation, Quebec. *Canadian Journal Earth Science*, *19*(2), 267–287.

Hermanns, R. L., & Strecker, M. R. (1999). Structural and lithological controls on large Quaternary rock avalanches (sturzstroms) in arid northwestern Argentina. *Geological Society of America Bulletin*, *111*(6), 934–948.

Hilgen, F. J., Lourens, L. J., & Van Dam, J. A. (2012). The Neogene Period. In F. M. Gradstein, J. G. Ogg, M. K. Schmitz, G. M. Ogg (Eds.), *The geologic time scale 2012* (pp. 923–978). Amsterdam: Elsevier.

Hilley, G. E., & Strecker, M. R. (2004). Steady state erosion of critical Coulomb wedges with applications to Taiwan and the Himalaya. *Journal of Geophysical Research*, *109*(B1). https://doi.org/10.1029/2002JB002284

Hilley, G. E., Strecker, M. R., & Ramos, V. A. (2004). Growth and erosion of fold-and-thrust belts with an application to the Aconcagua fold-and-thrust belt, Argentina. *Journal of Geophysical Research*, *109*(B1). https://doi.org/10.1029/2002JB002282

Horton, B. K. (2012). Cenozoic evolution of Hinterland Basins in the Andes and Tibet. In C. Busby & A. Azor (Eds.), *Tectonics of sedimentary basins: Recent advances* (pp. 427–444). New York, NY: John Wiley & Sons, Ltd.

Horton, B. K., Hassanzadeh, J., Stockli, D. F., Axen, G. J., Gillis, R. J., Guest, B., et al. (2008). Detrital zircon provenance of Neoproterozoic to Cenozoic deposits in Iran: Implications for chronostratigraphy and collisional tectonics. *Tectonophysics*, *451*(1–4), 97–122. https://doi.org/10.1016/j.tecto.2007.11.063

Horton, K. B., & Schmitt, J. G. (1996). Sedimentology of a lacustrine fan-delta system, Miocene Horse Camp formation, Nevada, USA. *Sedimentology*, *43*(1), 133–155.

Hrouda, F. (1982). Magnetic anisotropy of rocks and its application in geology and geophysics. *Suveys in Geophysics*, *5*(1), 37–82.

Huang, B., Piper, J. D. A., Peng, S. H., Liu, T., Li, Z. H., Wang, Q., & Zhu, R. (2006). Magnetostratigraphic study of the Kuche Depression, Tarim Basin, and Cenozoic uplift of the Tian Shan range, western China. *Earth and Planetary Science Letters*, *251*(3–4), 346–364. https://doi.org/10.1016/j.epsl.2006.09.020

Ilgar, A., & Nemec, W. (2005). Early Miocene lacustrine deposits and sequence stratigraphy of the Ermenek Basin, Central Taurides, Turkey. *Sedimentary Geology*, *173*(1–4), 233–275. https://doi.org/10.1016/j.sedgeo.2003.07.007

Ingersoll, R. V., Bullaed, T. F., Ford, R. L., Grimm, J. P., Pickle, J. D., & Sares, S. W. (1984). The effect of grain size on detrital modes: A test of the Gazzi-Dickinson point-counting method. *Journal of Sedimentary Petrology*, *54*(1), 103–116.

Isacks, B. L. (1988). Uplift of the Central Andean Plateau and bending of the Bolivian Orocline. *Journal of Geophysical Research*, *93*(B4), 3211–3231.

Jimenez-Munt, I., Fernandez, M., Saura, E., Verges, J., & Garcia-Castellanos, D. (2012). 3-D lithospheric structure and regional/residual Bouger anomalies in the Arabia-Eurasia collision (Iran). *Geophysical Journal International*, *190*(3), 1311–1324. https://doi.org/10.1111/j.1365-246X.2012.05580.x

Keighiley, D. (2008). A lacustrine shoreface succession in the Albert Formation, Moncton Basin, New Brunswick. *Bulletin of Canadian Petroleum Geology*, *56*(4), 235–258. https://doi.org/10.2113/gscpgbull.56.4.235

Kirschvink, J. L. (1980). The least-squares line and plane and the analysis of palaeomagnetic data. *Geophysical Journal International*, *62*(3), 699–718.

Kodama, K. P. (2012). *Paleomagnetism of sedimentary rocks: Process and interpretation science*. John Wiley & Sons.

Koshnaw, R.I., Stockli, D.F., & Schlunegger, F., (2018). Timing of the Arabia-Eurasia continental collision—Evidence from detrital zircon U-Pb geochronology of the Red Bed Series strata of the northwest Zagros hinterland, Kurdistan region of Iraq. *Geology*, *47*(1), 47–50. https://doi.org/10.1130/G45499.1

Kraus, M. J. (1999). Paleosols in clastic sedimentary rocks: Their geologic applications. *Earth-Science Reviews*, *47*(1–2), 41–70.

Lamb, S., Hoke, L., Kennan, L., & Dewey, J. (1997). Cenozoic evolution of the Central Andes in Bolivia and northern Chile. In J. P Burg & M. Ford (Ed.), Orogeny through time (Vol. 121, pp. 237–264). Geological Society Special Publication.

Langereis, C. G., Krijgsman, W., Muttoni, G., & Menningning, M. (2010). Magnetostratigraphy-concepts, definitions, and applications. *Newsletter on Stratigraphy*, *43*(3), 207–233. http://10.1127/0078-0421/2010/0043-0207

Larrasoana, J. C., Pueyo, E. L., & Pares, J. M. (2004). An integrated AMS, structural, palaeo- and rock-magnetic study of Eocene marine marls from the Jaca-Pamplona basin (Pyrenees, N Spain); new insights into the timing of magnetic fabric acquisition in weakly deformed mudrocks. *Geological Society, London, Special Publications*, *238*(1), 127–143. https://doi.org/10.1144/GSL.SP.2004.238.01.10

Lowenstein, T. K., & Hardie, L. A. (1985). Criteria for the recognition of salt-pan evaporites. *Sedimentology*, *32*(5), 627–644.

Ludwig, K. R. (2003). User's Manual for Isoplot/Ex: A geochronological toolkit for Microsoft Excel (Vol. 4, p. 72). Berkeley Geochronology Center Special Publication.

Madanipour, S., Ehlres, T. A., Yassaghi, A., & Enkelmann, E. (2017). Accelerated middle Miocene exhumation of the Talesh Mountains constrained by U-Th/He thermochronometry: Evidence for the Arabia-Eurasia collision in the NW Iranian Plateau. *Tectonics*, *36*(8), 1538–1561. https://doi.org/10.1002/2016TC004291

Madanipour, S., Ehlres, T. A., Yassaghi, A., Rezaeian, M., Enkelmann, E., & Bahroudi, A. (2013). Synchronous deformation on orogenic plateau margins: Insights from the Arabia-Eurasia collision. *Tectonophysics*, *608*, 440–451. https://doi.org/10.1016/j.tecto.2013.09.003

Madanipour, S., Yassaghi, A., Ehlers, T. A., & Enkelmann, E. (2018). Tectonostratigraphy, structural, geometry and kinematics of the NW Iranian Plateau margin: Insight from the Talesh Mountains, Iran. *American Journal of Science*, *318*(2), 208–245. https://doi.org/10.2475/02.2018.02

Mahon, K. I. (1996). The New "York" regression: Application of an improved statistical method to geochemistry. *International Geology Review*, *38*(4), 293–303.

Maizels, J. (1989). Sedimentology, paleoflow dynamics and flood history of jokulhlaup deposits; paleohydrology of Holocene sediment sequences in southern Iceland sandur deposits. *Journal of Sedimentary Research*, *59*(2), 204–223.

Mattei, M., Cifelli, F., Alimohammaadian, H., & Rashid, H. (2020). The role of active strike-slip faults and opposite vertical axis rotations in accommodating Eurasia-Arabia shortening in Central Iran. *Tectonophysics*, *774*, 228243. https://doi.org/10.1016/j.tecto.2019.228243

Mattei, M., Cifelli, F., Alimohammaadian, H., Rashid, H., Winkert, A., & Sagnotti, L. (2017). Oroclinal bending in the Alborz Mountains (Northern Iran): New constraints on the age of South Caspian subduction and extrusion tectonics. *Gondwana Research*, *42*, 13–28. https://doi.org/10.1016/j.gr.2016.10.003

Mattei, M., Cifelli, F., Muttoni, G., & Rashid, H. (2015). Post-Cimmerian (Jurassic–Cenozoic) paleogeography and vertical axis tectonic rotations of Central Iran and the Alborz Mountains. *Journal of Asian Earth Sciences*, *102*, 92–101. https://doi.org/10.1016/j.jseaes.2014.09.038

Mattei, M., Visconti, L. A., Cifelli, F., Nozaem, R., Winkert, A., & Sagnotti, L. (2019). Clockwise paleomagnetic rotations in north-eastern Iran: Major implications on recent geodynamic evolution of outer sectors of the Arabia-Eurasia collision zone. *Gondwana Research*, *71*, 194–209. https://doi.org/10.1016/j.gr.2019.01.018

Mcfadden, P. L., & Mcelhinny, M. W. (1990). Classification of the reversal test in palaeomagnetism. *Geophysical Journal International*, *103*(3), 725–729.

Merrill, R. R., Mcfadden, P., & Mcelhinny, M. (1996). *The magnetic field of the Earth: Paleomagnetism, the core, and the deep mantle*. International geophysics series ISSN 0074-6142 (p. 531). San Diego: Academic Press.

Métivier, F., Gaudemer, Y., Tapponnier, P., & Meyer, B. (1998). Northeastward growth of the Tibetan plateau deduced from balanced reconstructions of two depositional areas: The Qaidam and Hexi Corridor basins, China. *Tectonics*, *17*(6), 823–842.

Meyer, B., Tappnnnier, P., Bourjot, L., Métivier, F., Gaudemer, Y., Peltzer, G., et al. (1998). Crustal thickening in Gansu-Qinghai, lithospheric mantle subduction, and oblique, strike-slip controlled growth of the Tibet plateau. *Geophysical Journal International*, *135*(1), 1–47.

Miall, A. D. (1978). Lithofacies types and vertical profile models in braided river deposits. *Fluvial Sedimentology: Canadian Society Petrology Geology Memoir*, *5*, 597–604.

Miall, A. D. (1985). Architectural-element analysis: A new method of facies analysis applied to fluvial deposits. *Earth-Science Reviews*, *22*(4), 261–308.

Miall, A. D. (1996). *The Geology of Fluvial Deposits* (Vol. 16, p. 582). Berlin: Springer Verlag.

Miall, A. D. (1997). A review of the braided river depositional environment. *Earth Science Review*, *13*(1), 1–62.

Monlar, P., England, P. H., & Martiod, J. (1993). Mantle dynamics, uplift of the Tibetan Plateau, and the Indian monsoon. *Reviews of Geophysics*, *31*(4), 357–396.

Morley, C., Kongwung, B., Julapour, A. A., Abdolghafourian, A., Hajian, M., Waples, D., et al. (2009). Structural development of the major late Cenozoic basin and transpressional belt in Central Iran: The Central Basin in the Qom-Saveh area. *Geosphere*, *5*(4), 325–362. https://doi.org/10.1130/GES00223.1

Motaghi, K., Ghods, A., Sobouti, F., Shabanian, E., Mahmoudabadi, M., & Priestly, K. (2018). Lithospheric seismic structure of the West Alborz – Talesh ranges, Iran. *Geophysical Journal International*, *215*(3), 1766–1780. https://doi.org/10.1093/gji/ggy372

Mouthereau, F., Lacombe, O., & Verges, J. (2012). Building the Zagros collisional orogen: Timing, strain distribution and the dynamics of Arabia/Eurasia plate convergence. *Tectonophysics*, *532–535*, 27–60. https://doi.org/10.1016/j.tecto.2012.01.022

Nabatian, G., Ghaderi, M., Neubauer, F., Honaemand, M., Liu, X., Dong, Y., et al. (2014). Petrogenesis of Tarom high-potassic granitoids in the Alborz-Azarbaijan belt, Iran: Geochemical, U-Pb zircon and Sr–Nd–Pb isotopic constraints. *Lithos*, *184–187*, 324–345. https://doi.org/10.1016/j.lithos.2013.11.002

Omrani, H., Moazzen, M., Oberhansli, R., Tsujimori, T., Bousquet, R., & Moayyed, M. (2013). Metamorphic history of glaucophane-paragonite-zoisite eclogites from the Shanderman area, northern Iran. *Journal of Metamorphic Geology*, *31*(8), 791–812. https://doi.org/10.1111/jmg.12045

Paknia, M. (2019). *An integrated paleomagnetic, rock magnetic, anisotropy of magnetic susceptibility, stratigraphic and structural study of Miocene synorogenic red beds from NW Iran: Insight into the geologic evolution of the intermontane Tarom Basin at the linkage between the western Alborz Mountains and the northern margin of the Iranian Plateau* (PhD thesis; chapter III, XXXII PhD cycle) Department of Science, University of Roma Tre.

Pares, J. M. (2004). How deformed are weakly deformed mudrocks? Insights from magnetic anisotropy. In F. Martin-Hernandez, C. Lüneburg, C. Aubourg, M. Jackson (Eds.), Magnetic fabrics: Methods and applications (Vol. 238, pp. 191–203). Geological Society, London, Special Publication.

Pingel, H., Alonso, R. N., Altenberger, U., Cottle, J., & Strecker, M. R. (2019a). Miocene to Quaternary basin evolution at the southeastern Andean Plateau (Puna) margin (ca. 24°S lat, Northwestern Argentina). *Basin Research*, *31*(4), 808–826. https://doi.org/10.1111/bre.12346

Pingel, H., Schildgen, T., Strecker, M. R., & Wittmann, H. (2019b). Pliocene–Pleistocene orographic control on denudation in northwest Argentina. *Geology*, *47*(4), 359–362. https://doi.org/10.1130/G45800.1

Pirouz, M., Avouzc, J.-P., Hassanzadeh, J., Kirschvink, J. L., & Bahroudi, A. (2017). Early Neogene foreland of the Zagros, implications for the initial closure of the Neo-Tethys and kinematics of crustal shortening. *Earth and Planetary Science Letters*, *477*, 168–182. https://doi.org/10.1016/j.epsl.2017.07.046

Puy-Aquiza, M. J., Mirand-Aviles, R., Garcia-Barragan, J. C., Loza-Aguirre, I., Li, Y., & Anazanor, G. (2017). Facies analysis, stratigraphic architecture and depositional environments of the Guanajuato conglomerate in the Sierra de Guanajuato, Mexico. *Boletín de la Sociedad Geológica Mexicana*, *69*(2), 385–408. https://doi.org/10.18268/bsgm2017v69n2a5

Rabiee, A., Rossetti, F., Asahara, Y., Azizi, H., Glodny, J., Lucci, F., et al. (2020). Long-lived, Eocene-Miocene stationary magmatism in NW Iran along a transform plate boundary, NW Iran. *Gondwana Research*, *85*, 237–262. https://doi.org/10.1016/j.gr.2020.03.014

Rahmani, M., Motaghi, K., Ghods, A., Sobouti, F., Talebian, M., Ai, Y., & Chen, L. (2019). Deep velocity image of the north Zagros collision zone (Iran) from regional and teleseismic tomography. *Geophysical Journal International*, *219*(3), 1729–1740. https://doi.org/10.1093/gji/ggz393

Reiners, P. W., & Brandon, M. T. (2006). Using thermochronology to understand orogenic erosion. *Annual Review of Earth and Planetary Sciences*, *34*, 419–466. https://doi.org/10.1146/annurev.earth.34.031405.125202

Reuter, M., Piller, W. E., Harzhauser, M., Mandic, O., Berning, B., & Rogl, F. (2009). The Oligo-/Miocene Qom Formation (Iran): Evidence for an early Burdigalian restriction of the Tethyan Seaway and closure of its Iranian gateways. *International Journal of Earth Sciences*, *98*(3), 627–650. https://doi.org/10.1007/s00531-007-0269-9

Rezaeian, M., Carter, A., Hovius, N., & Allen, M. B. (2012). Cenozoic exhumation history of the Alborz Mountains, Iran: New constraints from low-temperature chronometry. *Tectonics*, *31*(2), TC2004. https://doi.org/10.1029/2011TC002974

Ridgway, K. D., & De Celles, P. G. (1993). Stream-dominated alluvial fan and lacustrine depositional systems in Cenozoic strike-slip basins, Denali fault system, Yukon Territory, Canada. *Sedimentology*, *40*(4), 645–666.

Rieben, H. (1955). The geology of the Tehran plain. *American Journal of Science*, *253*(11), 617–639.

Robert, A. M. M., Letouzey, J., Kavoosi, M. A., Sherkati, S. H., Muller, C., Vergés, J., & Aghababaei, A. (2014). Structural evolution of the Kopeh Dagh fold-and-thrust belt (NE Iran) and interactions with the South Caspian Sea Basin and Amu Darya Basin. *Marine and Petroleum Geology*, *57*, 68–87. https://doi.org/10.1016/j.marpetgeo.2014.05.002

Robion, P., Grelaud, S., & Frizon de lamotte, D. (2007). Pre-folding magnetic fabrics in fold and-thrust belts: Why the apparent internal deformation of the sedimentary rocks from the Minervois basin (NE-Pyrenees, France) is so high compared to the Potwar basin (SW-Himalaya, Pakistan)? *Sedimentary Geology*, *196*(1–4), 181–200. https://doi.org/10.1016/j.sedgeo.2006.08.007

Royde, L. H., Burchfiel, B. C., King, R. W., Wang, E., Chen, Z., Shen, F., & Liu, Y. (1997). Surface deformation and lower crustal flow in eastern Tibet. *Science*, *276*(5313), 788–790.

Royden, L. (1996). Coupling and decoupling of crust and mantle in convergent orogens: Implications for strain partitioning in the crust. *Journal of Geophysical Research*, *101*(B8), 17679–17705.

Saint-Bezar, B., Hebert, R. L., Aubourg, C., Robion, P., Swenen, R., & De Lamotte, D. F. (2002). Magnetic fabric and petrographic investigations of hematite-bearing sandstones within ramp-related folds: Examples from the South Atlas front (Morocco). *Journal of Structural Geology*, *24*(9), 1507–1520. https://doi.org/10.1016/S0191-8141(01)00140-7

Schildgen, T. F., Robinson, R. A. J., Savi, S., Phillips, W. M., Spemcer, J. Q. G., Bookhangen, B., et al. (2016). Landscape response to late Pleistocene climate change in NW Argentina: Sediment flux modulated by basin geometry and connectivity. *Journal of Geophysical Research*, *121*(2), 392–414. https://doi.org/10.1002/2015JF003607

Schildgen, T. F., Yildirim, C., Cosentino, D., & Strecker, M. R. (2014). Linking slab break-off, Hellenic trench retreat, and uplift of the Central and Eastern Anatolian plateaus. *Earth-Science Reviews*, *128*, 147–168. https://doi.org/10.1016/j.earscirev.2013.11.006

Schmitt, A. K., Grove, M., Harrison, T. M., Lovera, O. M., Hulen, J., & Waters, M. (2003). The Geysers–Cobb Mountain magma system, California (Part 1): U-Pb zircon ages of volcanic rocks, conditions of zircon crystallization and magma residence times. *Geochimica et Cosmochimica Acta*, *67*(18), 3423–3442. https://doi.org/10.1016/S0016-7037(03)00140-6

Siks, B. C., & Horton, B. K. (2011). Growth and fragmentation of the Andean foreland basin during eastward advance of fold-thrust deformation, Puna plateau and Eastern Cordillera, northern Argentina. *Tectonics*, *30*(6). https://doi.org/10.1029/2011TC002944

Sobel, E. R., Hilley, G. E., & Strecker, M. R. (2003). Formation of internally drained contractional basins by aridity-limited bedrock incision. *Journal of Geophysical Research*, *108*(B7), JB001883. https://doi.org/10.1029/2002JB001883

Sobel, E. R., & Strecker, M. R. (2003). Uplift, exhumation and precipitation: Tectonic and climatic control of Late Cenozoic landscape evolution in the northern Sierras Pampeanas, Argentina. *Basin Research*, *15*(4), 431–451. https://doi.org/10.1046/j.1365-2117.2003.00214.x

Soto, R., Larrasoana, J. C., Arlegui, L. E., Beamud, E., Olivaurcia, B., & Simon, J. L. (2009). Reliability of magnetic fabric of weakly deformed mudrocks as a palaeostress indicator in compressive settings. *Journal of Structural Geology*, *31*(5), 512–522. https://doi.org/10.1016/j.jsg.2009.03.006

Stanistreet, I. G., & McCarthy, T. S. (1993). The Okavango Fan and the classification of subaerial fan systems. *Sedimentary Geology*, *85*(1–4), 115–133.

Stocklin, J., & Eftekharnezhad, J. (1969). *Geological map of Zanjan quadrangle*. Tehran: Geological Survey of Iran.

Strecker, M. R., Alonso, R., Bookhagen, B., Carrpapa, B., Coutand, I., Hain, M. P., et al. (2009). Does the topographic distribution of the central Andean Puna Plateau result from climatic or geodynamic processes? *Geology*, *37*(7), 643–646. https://doi.org/10.1130/G25545A.1

Strecker, M. R., Alonso, R. N., Bookhagen, B., Carrpapa, B., Hilley, G. E., Sobel, E. R., & Ttruth, M. H. (2007). Tectonics and climate of the southern central Andes. *Annual Review of Earth and Planetary Sciences*, *35*, 747–787. https://doi.org/10.1146/annurev.earth.35.031306.140158

Streit, R. L., Burbank, D. W., Strecker, M. R., Alonso, R. N., Cottle, J. M., & Kulander-Clark, A. R. C. (2015). Controls on intermontane basin filling, isolation and incision on the margin of the Puna Plateau, NW Argentina (~23°S). *Basin Research*, *29*(S1), 131–155. https://doi.org/10.1111/bre.12141

Tadayon, M., Rosseti, F., Zattin, M., Calzolari, G., Nozaem, R., Salvini, F., et al. (2018). The long-term evolution of the Doruneh fault region (Central Iran): A key to understanding the spatio-temporal tectonic evolution in the hinterland of the Zagros convergence zone. *Geological Journal*, *54*(3), 1454–1479. https://doi.org/10.1002/gj.3241

Tarling, D. H., & Hrouda, F. (1993). *The magnetic anisotropy of rocks* (p. 217). London: Chapman & Hall.

Tauxe, L., Kylstra, N., & Constable, C. (1991). Bootstrap statistics for paleomagnetic data. *Journal of Geophysical Research: Solid Earth*, *96*(B7), 11723–11740. https://doi.org/10.1029/91JB00572

Tauxe, L., & Watsonb, G. S. (1994). The fold test: an eigen analysis approach. *Earth and Planetary Science Letters*, *122*(3–4), 331–341. https://doi.org/10.1016/0012-821X(94)90006-X

Tha, H. V., Wysocka, A., Pha, P. D., Cuong, N. Q., & Ziolkowski, P. (2015). Lithofacies and depositional environments of the Paleogene/Neogene sediments in the Hoanh Bo Basin (Quang Ninh province, NE Vietnam). *Geology, Geophysics and Environment*, *41*(4), 353–369. http://10.0.29.70/geol.2015.41.4.353

Thiede, R., Bookhangen, B., Arrowsmith, J. R., Sobel, E., & Strecker, M. R. (2004). Climatic control on rapid exhumation along the Southern Himalayan Front. *Earth and Planetary Science Letters*, *222*(3–4), 791–806. https://doi.org/10.1016/j.epsl.2004.03.015

Todd, S. P. (1989). Stream-driven, high-density gravelly traction carpets: Possible deposits in the Trabeg conglomerate formation, SW Ireland and some theoretical considerations of their origin. *Sedimentology*, *36*(4), 513–735.

Tofelde, S., Schildgen, T. F., Savi, S., Pingel, H., Wickert, A. D., Bookhangen, B., et al. (2017). 100 kyr fluvial cut-and-fill terrace cycles since the Middle Pleistocene in the southern Central Andes, NW Argentina. *Earth and Planetary Science Letters*, *473*, 141–153. https://doi.org/10.1016/j.epsl.2017.06.001

Uba, C. E., Heubeck, C., & Hulka, C. (2005). Facies analysis and basin architecture of the Neogene Subandean synorogenic wedge, southern Bolivia. *Sedimentary Geology*, *180*(3), 91–123. https://doi.org/10.1016/j.sedgeo.2005.06.013

Verdel, C., Wernicke, B. P., Hassanzadeh, J., & Guest, B. (2011). A Paleogene extensional arc flare-up in Iran. *Tectonics*, *30*, TC3008(3), https://doi.org/10.1029/2010TC002809

Vernant, P., Nilforoushan, F., Hatzfeld, D., Abbassi, M. R., Vigny, C., Masson, F., et al. (2004). Present-day crustal deformation and plate kinematics in the Middle East constrained by GPS measurements in Iran and northern Oman. *Geophysical Journal International*, *157*(1), 381–398. https://doi.org/10.1111/j.1365-246X.2004.02222.x

Vincent, S. J., Morton, A. C., Carter, A., Gibbs, S., & Barabadze, T. G. (2007). Oligocene uplift of the Western Greater Caucasus: An effect of initial Arabia–Eurasia collision. *Terra Nova*, *19*(2), 160–166. https://doi.org/10.1111/j.1365-3121.2007.00731.x

Whippe, K. X., & Meade, B. J. (2004). Controls on the strength of coupling among climate, erosion, and deformation in two-sided, frictional orogenic wedges at steadystate. *Journal of Geophysical Research*, *109*(F1). https://doi.org/10.1029/2003JF000019

Willett, S. D. (1999). Orogeny and orography: The effects of erosion on the structure of mountain belts. *Journal of Geophysical Research*, *104*(B12), 28957–28981.

Wilmsen, M., Fursichfranz, F. T., Fursich, T., Seyed-Emami, K., Majidifard, M. R., & Taheri, J. (2009). The Cimmerian Orogeny in northern Iran: Tectono-stratigraphic evidence from the foreland. *Terra Nova*, *21*(3), 211–218. https://doi.org/10.1111/j.1365-3121.2009.00876.x

Yassaghi, A., & Madanipour, S. (2008). Influence of a transverse basement fault on along strike variations in the geometry of an inverted normal fault: Case study of the Mosha Fault, Central Alborz Range, Iran. *Journal of Structural Geology*, *30*(12), 1507–1519. https://doi.org/10.1016/j.jsg.2008.08.006

Zanchi, A., Zanchetta, S., Berra, F., Mattei, M., Garzanti, E., Molyneux, S., et al. (2009). The Eo-Cimmerian (Late? Triassic) orogeny in North Iran. *Geological Society, London, Special Publication*, *312*(1), 31–55. https://doi.org/10.1144/SP312.3

Zhu, R. X., Potts, R., Pan, Y. X., Lu, L. Q., Yao, H. T., Deng, C. L., & Qin, H. F. (2008). Paleomagnetism of the Yuanmou Basin near the southeastern margin of the Tibetan Plateau and its constraints on late Neogene sedimentation and tectonic rotation. *Earth and Planetary Science Letters*, *272*(1–2), 97–104. https://doi.org/10.1016/j.epsl.2008.04.016

Zijderveld, J. D. A. (1967). A. C. demagnetization of rocks—Analysis of results. In D. W. Collinson et al. (Eds.), *Methods in Paleomagnetism* (pp. 254–286). New York, NY: Elsevier.